

Comparison between the Predictions of Diffusion-Reaction Models and Localized Ca^{2+} Transients in Amphibian Skeletal Muscle Fibers

David Novo, Marino DiFranco, and Julio L. Vergara

Department of Physiology, UCLA School of Medicine, Los Angeles, California

ABSTRACT We developed a three-dimensional cylindrical diffusion-reaction model of a single amphibian myofibril in which Ca^{2+} release occurred only at the Z-line. The model incorporated diffusion of Ca^{2+} , Mg^{2+} , and all relevant buffer species, as well as the kinetic binding reactions between the buffers and appropriate ions. Model data was blurred according to a Gaussian approximation of the point spread function of the microscope and directly compared with experimental data obtained using the confocal spot methodology. The flux parameters were adjusted until the simulated Z-line transient matched the experimental one. This model could not simultaneously predict key parameters of the experimental M- and Z-line transients, even when model parameters were adjusted to unreasonably extreme values. Even though the model was accurate in predicting the Z-line transient under conditions of high [EGTA], it predicted a significantly narrower Ca^{2+} domain than observed experimentally. We modified the model to incorporate a broader band of release centered at the Z-line. This extended release model was superior both in simultaneously predicting critical features of the Z- and M-line transients as well as the domain profile under conditions of high [EGTA]. We conclude that a model of release occurring exclusively at the Z-line cannot explain our experimental data and suggest that Ca^{2+} may be released from a broader region of the sarcoplasmic reticulum than just the T-tubule-sarcoplasmic reticulum junction.

INTRODUCTION

The development of tension in skeletal muscle depends on the binding of Ca^{2+} to the troponin complex which allows the thick and thin filaments to interact. Since this complex is located in a specific subregion of the sarcomere, understanding the spatiotemporal profile of the calcium concentration ($[\text{Ca}^{2+}]$) changes within the muscle fiber is crucial to understanding the excitation-contraction (EC) coupling process.

Traditionally, $[\text{Ca}^{2+}]$ changes in response to physiological action potential (AP) stimulation have been measured in muscle fibers using techniques that report Ca^{2+} -dependent fluorescence signals from regions that span many sarcomeres (global Ca^{2+} transients; Kim and Vergara, 1998; Vergara et al., 1991); see Rios and Pizarro (1991) for a review. However, these Ca^{2+} transients report a mix of fluorescence contributions from regions of the sarcomere that have marked differences in $[\text{Ca}^{2+}]$, resulting in a spatially averaged signal that provides no information about the spatial distribution of the $[\text{Ca}^{2+}]$ changes (Escobar et al., 1994). The most relevant information about the Ca^{2+} signaling during EC coupling can only be obtained from measurements of intrasarcomeric Ca^{2+} gradients, which require localized (confocal) detection of fluorescence signals from small regions within the sarcomere. To obtain this information, we developed the confocal spot technique (Escobar et al., 1994; Vergara et al., 2001; DiFranco et al.,

2002), which allows us to measure the $[\text{Ca}^{2+}]$ in a $0.3\text{-}\mu\text{m}$ confocal spot in a single myofibril. An AP is elicited and a localized fluorescence transient is recorded from a single spot position. A complete high resolution spatiotemporal profile of the $[\text{Ca}^{2+}]$ distribution within a single sarcomere is obtained by recording several transients at different spot positions located at 200-nm intervals along the fiber axis (DiFranco et al., 1999; Vergara et al., 2001).

The magnitude and time-course of the $[\text{Ca}^{2+}]$ gradients depend on many factors:

1. The magnitude and time-course of the Ca^{2+} release flux from the sarcoplasmic reticulum (SR),
2. The geometry and extent of the Ca^{2+} release sites,
3. The interaction of Ca^{2+} with Ca^{2+} buffers, and
4. The magnitude and time-course of the removal of Ca^{2+} by the SR Ca^{2+} ATPase.

It is currently believed that Ca^{2+} is released from the terminal cisternae of the SR into the $\sim 16\text{-nm}$ cleft where the SR abuts the T-tubule (T-SR junction) and then diffuses throughout the myofibril, all the while interacting with endogenous Ca^{2+} buffers until it is removed by the SR Ca^{2+} ATPase (Franzini-Armstrong et al., 1998). However, recent evidence suggests that that release site may be broader than just the T-SR junction (Vergara et al., 2001; DiFranco et al., 2002). The interaction of Ca^{2+} with buffers is a particularly complex phenomenon because all buffers can bind to Ca^{2+} , thus tending to diminish the free $[\text{Ca}^{2+}]$; but in addition, mobile buffers can also carry Ca^{2+} to regions of the fiber that it would not have reached otherwise.

To evaluate the role of buffers and the magnitude and location of the SR Ca^{2+} release in light of data obtained using confocal detection techniques, we present a three-dimensional cylindrical diffusion-reaction model that is an

Submitted May 30, 2002, and accepted for publication April 16, 2003.

Address reprint requests to Julio Vergara, Dept. of Physiology, UCLA School of Medicine, 10833 Le Conte Avenue 53-263 CHS, Los Angeles, CA 90095-1751. Tel.: 310-825-9307; Fax: 310-206-3788; E-mail: jvergara@mednet.ucla.edu.

© 2003 by the Biophysical Society

0006-3495/03/08/1080/18 \$2.00

extension of previous myofibrillar models (Cannell and Allen, 1984; Baylor and Hollingworth, 1998). In our model, Ca^{2+} ions were released into the myofibril from its periphery (outermost 16 nm) either only at the Z-line, which represents the T-SR junction at this location, or from an extended release site. Ca^{2+} and Mg^{2+} ions were allowed to diffuse throughout the myofibril. All relevant mobile buffers—EGTA, Oregon Green 488 BAPTA-5N (OGB-5N), parvalbumin, and ATP—interacted with Ca^{2+} (and Mg^{2+} when relevant) according to their kinetic binding characteristics and were also allowed to diffuse. The $[\text{Ca}^{2+}]$ -dependent fluorescence of the indicator OGB-5N was calculated according to its properties and the resulting fluorescence was blurred by convolving it with a triple Gaussian approximation of the point spread function (PSF) of the microscope objective. Simulated fluorescence domains were then constructed by assuming that there was a pinholed detector in the image plane of the microscope that measured a localized transient every 200 nm. These simulated domains were then directly compared with experimental ones obtained from fibers stretched to 4- μm sarcomere spacing to determine how well the model was able to predict the experimental observations.

We have found that the currently accepted view of Ca^{2+} release occurring only at the Z-line and dispersing throughout the myofibril solely by diffusion is not compatible with measurements obtained using the confocal spot technique. Several key parameters could not be predicted, including the time-course and magnitude of the M-line transient, the delay before fluorescence that is first observed at the M-line, and the width of the domain observed under conditions of high [EGTA]. By extending the release site most of these discrepancies were minimized.

Parts of the model comparisons presented in this article have previously been published in abstract form (Novo et al., 2001, 2002).

METHODS

Confocal spot detection

Experimental traces used to compare to model simulations were obtained using a confocal spot detection methodology, described in detail previously (Escobar et al., 1994; Vergara et al., 2001; DiFranco et al., 2002). Briefly, a single muscle fiber from the dorsal head of the *semitendinosus* muscle of the frog *Rana catesbeiana* was mounted in a double Vaseline gap chamber situated on a custom made stage scanning inverted confocal microscope (DiFranco et al., 1999; Vergara et al., 2001; DiFranco et al., 2002). Both ends of the muscle fiber were soaked in an internal solution containing the Ca^{2+} indicator dye OGB-5N (Molecular Probes, Eugene, OR). In experiments with high (either 10 or 20 mM) [EGTA], the fiber was first loaded with 0.5 mM EGTA and transients were acquired as described in DiFranco et al. (1999, 2002) and Vergara et al. (2001). The high [EGTA] was then added to the cut ends along with Ca^{2+} such that the free $[\text{Ca}^{2+}]$ was 0.1 μM , and allowed to equilibrate for 30 min before transients were recorded.

Given that the dimensions of the confocal spot (see below) are smaller than the diameter of a frog myofibril, it is reasonable to assume that our fluorescence records arise from a single myofibril (DiFranco et al., 2002).

Thus, our model, which is designed to generate data that can be quantitatively compared to the experimental data, is an extension of the single myofibril cylindrical scheme proposed by Cannell and Allen in 1984. In our model, Ca^{2+} ions are either released only at the Z-line or from an extended release band and then diffuse throughout the myofibril, all the while interacting with the various Ca^{2+} binding species. Based upon the formation of Ca^{2+} -dye complex at different radial and longitudinal positions, localized fluorescence transients are calculated after considering the blurring introduced by the point-spread function (PSF) of the optical system (see below). When these signals are expressed in terms of $\Delta F/F$ (see below), they can be directly compared with the experimental data.

Model geometry

The half-sarcomere of a frog single myofibril is represented as a radially symmetrical cylinder with the positional variables being r , the radial coordinate, ranging from 0 to a from the center to the edge of the myofibril, and x , the longitudinal coordinate, ranging from 0 to l from the Z-line to the M-line (Fig. 1 A). Because of the symmetry within a single myofibril it is assumed that there is no net longitudinal flux of Ca^{2+} at the M-line ($x = l$). In addition, because of symmetry with other myofibrils, it is assumed that there is no net flux of Ca^{2+} in or out of the myofibril except at the Ca^{2+} release sites and SR Ca^{2+} pump (Fig. 1 B). It is also assumed that the myofibril is an isotropic volume in which all molecules can freely diffuse, with a mobility determined by their diffusion coefficients, in any direction (subject to the boundaries of the model).

The radial symmetry of the cylinder allows it to be mapped in the plane shown in Fig. 1 B. This plane is subdivided into a matrix of $m \times n$ voxels, where m represents the number of longitudinal voxels and n is the number of radial voxels. The width of the voxels in the radial direction was set equal to that in the longitudinal direction, with typical values for m and n being 128 and 32, respectively (Table 1). The voxel width was set to be ~ 16 nm so that the release site's longitudinal dimension is comparable to the spacing of the amphibian T-SR junction (Franzini-Armstrong, 1975, 1971; Peachey, 1965). It should be noted that because of the cylindrical geometry and the equal radial spacing used in the model, the voxel volumes at different radial shells are not equal. This is taken into account when calculating concentrations in a given voxel position.

Resting Ca^{2+} and Mg^{2+} concentrations

The resting $[\text{Ca}^{2+}]$, at the start of the simulation, was assumed to be 0.1 μM . The resting myofibrillar $[\text{Mg}^{2+}]$ was assumed to be equal to that in the cut end pools. This latter concentration was calculated as shown in Appendix A by solving the standard equilibrium binding equation with the parameters in Table 2 and assuming that ATP is the only Mg^{2+} chelator in the pools and that it also binds Ca^{2+} .

Ca^{2+} release

In the Z-line release model, Ca^{2+} is released into the sarcomere from voxel 1 in Fig. 1 B and Table 3, which corresponds to a narrow continuous ring of release surrounding the myofibril at the Z-line. In the extended release model, Ca^{2+} was released into the myofibril from voxel 1 plus a variable number of voxels denoted by 2 in Fig. 1 B and Table 3.

Although either model could implement any Ca^{2+} -release driving function, to simulate the release process in response to an AP, we used an exponential rising and falling function described by the equation

$$J(t) = J_{\max} (1 - e^{-t/\tau_{\text{on}}}) e^{-t/\tau_{\text{off}}} \quad (1.1)$$

The specific values for J_{\max} , τ_{on} , and τ_{off} were obtained by varying them until the time course of the simulated fluorescence transient at the Z-line matched a typical experimental Z-line transient. $J(t)$ is in units of *pmoles*

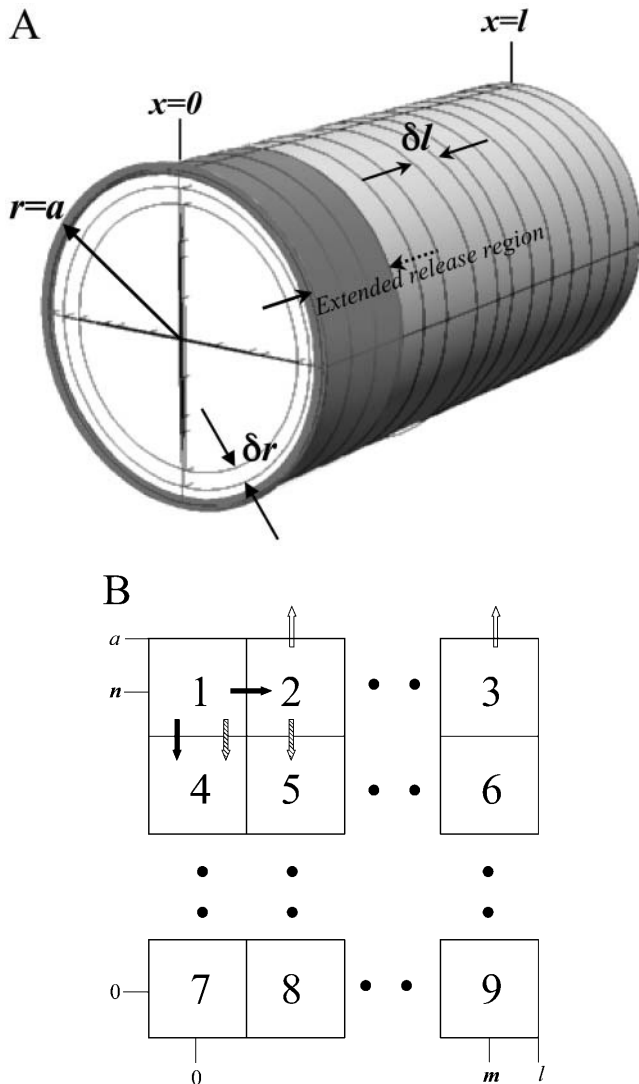


FIGURE 1 Schematic diagrams of simulated myofibril. (A) Model geometry of the cylindrical representation of a half-sarcomere. Ca^{2+} is released at the periphery of the myofibril either at the Z-line (dark ring at $x = 0$, $r = a$), or in an extended release region (darker shaded area). Dotted arrow denotes that the extended release region can be of a variable length. A typical simulation used 32 radial (δr) and 128 longitudinal (δl) segments. (B) Voxel types present in the myofibrillar model. The numbers indicate which diffusion-reaction equation from Table 3 applies to a given voxel position. In the Z-line release model, Ca^{2+} enters the myofibril through channels located on the boundaries between voxels 1 and 2 and between 1 and 4 (solid arrows). In the extended release model, Ca^{2+} enters the myofibril from voxel 1 and a variable number of voxels 2 (hatched arrows). Ca^{2+} exits via the SR ATPase located in voxels 2 and 3 (unfilled arrows). The dots represent repeats of the voxel type in the longitudinal (horizontal dots) or radial (vertical dots) directions. Typical values for m and n are 128 and 32, respectively. a represents the radius and l represents the length of the half-sarcomere, 0.5 and 2 μm , respectively.

($\text{cm}^2 \times \text{ms}$), in which the cm^2 refers to the cross-sectional area across which the flux is occurring. The entire magnitude of the flux applies to the half-sarcomere. In the extended release model, the flux (Eq. 1.1) was identical in all release voxels. To attain this function, the $[\text{Ca}^{2+}]$ increment at each time-step was calculated by considering the flux, outer surface area, and volume of each release voxel. When the extended flux simulations were constrained

to release Ca^{2+} only from voxel 1 in Fig. 1 B, the flux required to simulate the experimental Z-line transients was identical to the Z-line release model (data not shown).

Diffusion reaction scheme

The general diffusion-reaction equation that describes the rate of change of reactant concentration at any point is

$$\frac{\partial c_p}{\partial t} = D_p \nabla^2 c_p + W_p, \quad (1.2)$$

where c_p is the concentration of a reactant p at a given coordinate (r , x), $D_p \nabla^2 c_p$ represents the diffusional component of the rate of change of this reactant's concentration, and W_p is the binding reaction with other molecular species and the transport via the SR (if applicable). The model involves the simultaneous integration of multiple equations of the type of Eq. 1.2 for Ca^{2+} , Mg^{2+} , and the bound and free forms of each buffer in the system.

Diffusion

In the first term of Eq. 1.2, D_p represents the diffusion coefficient of the p^{th} molecular species and ∇^2 is the Laplace operator (Crank, 1975). After expressing the ∇^2 operator in cylindrical coordinates, Eq. 1.2 becomes

$$\frac{\partial c_p}{\partial t} = \frac{1}{r} \left[\frac{\partial}{\partial r} \left(r D_p \frac{\partial c_p}{\partial r} \right) + \frac{\partial}{\partial x} \left(r D_p \frac{\partial c_p}{\partial x} \right) \right] + W_p, \quad (1.3)$$

where r is the radial variable and x is the longitudinal variable.

To simplify the calculations, one can make the following transformations into dimensionless variables:

$$T_p = \frac{D_p t}{a^2}, \quad (1.4)$$

$$R = \frac{r}{a}, \quad (1.5)$$

$$X = \frac{x}{a}. \quad (1.6)$$

Substituting Eqs. 1.4–1.6 in Eq. 1.3 yields the simplified equation (Crank, 1975),

$$\frac{\partial c_p}{\partial T_p} = \frac{1}{R} \frac{\partial c_p}{\partial R} + \frac{\partial^2 c_p}{\partial R^2} + \frac{\partial^2 c_p}{\partial X^2} + W_p. \quad (1.7)$$

Henceforth, c_1 and c_2 will represent the free $[\text{Ca}^{2+}]$ and $[\text{Mg}^{2+}]$, respectively.

Reaction term for Ca^{2+} buffers

The model supports an arbitrary number of Ca^{2+} buffers. For simplicity, we have considered that each buffer only has a single binding site for which Ca^{2+} and Mg^{2+} can compete. Thus, there are up to three distinct forms for each buffer (free, Ca^{2+} -bound, and Mg^{2+} -bound) whose concentrations are considered a distinct c_p obeying Eq. 1.7. Therefore a buffer is completely defined by its diffusion coefficient, kinetic rate constants for binding Ca^{2+} and Mg^{2+} , initial concentration, and initial distribution (i.e., the buffer could be nonhomogeneously distributed within the myofibril). The Ca^{2+} -bound, Mg^{2+} -bound, and free form of the buffer all diffused independently of each other. At the start of the simulation the buffer was assumed to be at kinetic equilibrium with the free Ca^{2+} and Mg^{2+} . If the buffer only bound Ca^{2+} , the initial concentration of Ca^{2+} -bound buffer (e.g., c_{3c} for OGB-5N) is given by

TABLE 1 Parameters used in model simulations

Parameter	Symbol	Value	Reference
Half-sarcomere length	l	2 μm	DiFranco et al. (2002)
Myofibril radius	a	0.5 μm	
Number of radial segments	n	32	
Number of longitudinal segments	m	128	
T-tubule area: fiber volume		0.22 $\mu\text{m}^2/\mu\text{m}^3$	Eisenberg (1983)
Nonjunctional SR area: fiber volume		1.49 $\mu\text{m}^2/\mu\text{m}^3$	Eisenberg (1983)
Resting $[\text{Ca}^{2+}]$	$c_1(0)$	0.1 μM	
Ca^{2+} diffusion coefficient	D_1	$2 \times 10^{-6} \text{ cm}^2/\text{s}$	
SR pump density		30,000 pumps/ μm^2 SR	Franzini-Armstrong and Ferguson (1985)
SR pump k_m		0.22 μM	Vilsen and Andersen (1992)
SR pump turnover rate		7.6 Ca^{2+} ions/s	Vilsen and Andersen (1992)
SR pump V_{max}		9.7 $\mu\text{M}/\text{ms}$	Calculated
Pinhole width		50 μm	DiFranco et al. (2002)
Pinhole step size		0.2 μm	DiFranco et al. (2002)
PSF FWHM x - y	σ_{xy}	0.3 μm	
PSF FWHM z	σ_z	0.75 μm	

$$c_{3c}(0) = \frac{c_{3\text{tot}}c_1(0)}{K_c^{\text{OGB-5N}} + c_1(0)}, \quad (1.8)$$

where $c_{3\text{tot}}$ is the total dye concentration, $K_c^{\text{OGB-5N}}$ is the equilibrium dissociation constant for the reaction of the dye with Ca^{2+} , and $c_1(0)$ is the $[\text{Ca}^{2+}]$ at the start of the simulation (0.1 μM).

If the buffer binds both Ca^{2+} and Mg^{2+} , the initial concentration of the buffer species can be calculated, considering that

$$K_c^{\text{B}} = \frac{c_1c_{\text{Bf}}}{c_{\text{Bc}}}; \quad K_m^{\text{B}} = \frac{c_2c_{\text{Bf}}}{c_{\text{Bm}}}; \quad B_{\text{tot}} = c_{\text{Bf}} + c_{\text{Bc}} + c_{\text{Bm}},$$

and are given by

$$c_{\text{Bc}}(0) = \frac{c_1B_{\text{tot}}}{K_c^{\text{B}} \left(1 + \frac{c_1}{K_c^{\text{B}}} + \frac{c_2}{K_m^{\text{B}}} \right)}, \quad (1.9)$$

$$c_{\text{Bm}}(0) = \frac{c_2B_{\text{tot}}}{K_m^{\text{B}} \left(1 + \frac{c_1}{K_c^{\text{B}}} + \frac{c_2}{K_m^{\text{B}}} \right)}. \quad (1.10)$$

The notation for Eqs. 1.9 and 1.10 is presented in Appendix A.

The sole component of the W_p term in Eq. 1.7 for buffers is their binding to Ca^{2+} and Mg^{2+} . The rate of change of free Ca^{2+} as a result of interactions with a Ca^{2+} buffer (e.g., from OGB-5N), is described by

$$\frac{dc_1}{dt}(\text{OGB-5N}) = k_{-c}^{\text{OGB-5N}}c_{3c} - k_{+c}^{\text{OGB-5N}}c_{3f}c_1, \quad (1.11)$$

where $k_{+c}^{\text{OGB-5N}}$ and $k_{-c}^{\text{OGB-5N}}$ are the kinetic association and dissociation rate constants, respectively, for the interaction of OGB-5N with Ca^{2+} . Conversely, the reaction term for the bound form of the buffer (e.g., c_{3c} for OGB-5N) is equal to

$$-\frac{dc_1}{dt}(\text{OGB-5N}).$$

Reaction term for Mg^{2+}

The reaction term for Mg^{2+} represents the change in $[\text{Mg}^{2+}]$ due to its interaction with Mg^{2+} -binding buffers. The only two buffers for which this was considered were parvalbumin and ATP. The change in free $[\text{Mg}^{2+}]$ (e.g., from ATP) is described by:

$$\frac{dc_2}{dt}(\text{ATP}) = k_{-m}^{\text{ATP}}c_{5m} - k_{+m}^{\text{ATP}}c_{5f}c_2. \quad (1.12)$$

In the case of a buffer that bound both Ca^{2+} and Mg^{2+} , the change in free buffer was equal to the sum of Eqs. 1.11 and 1.12.

Reaction term for Ca^{2+}

Since Ca^{2+} interacts with all the buffers in the system as well as with the SR Ca^{2+} -ATPase, the W_1 term is the sum of two components. The first, Q_1 , represents the change in free $[\text{Ca}^{2+}]$ due to binding to buffers. This term is equal to the sum of all the Ca^{2+} components of the reaction terms for the free buffers of the form of Eq. 1.11. Thus,

$$Q_1 = W_3 + W_4 + W_{5c} + W_{6c} + W_7. \quad (1.13)$$

TABLE 2 Buffer parameters used in the model simulations

Buffer	k_{+c}^{B} ($\mu\text{M}^{-1} \text{ms}^{-1}$)	k_{-c}^{B} (ms^{-1})	k_{+m}^{B} ($\mu\text{M}^{-1} \text{ms}^{-1}$)	k_{-m}^{B} (ms^{-1})	Concentration (μM)	Diffusion Coefficient ($\text{cm}^2 \text{s}^{-1}$)	Ref
OGB-5N (c_{3f} , c_{3c})	1.7×10^{-1}	5.6	None	None	500	1.4×10^{-6}	DiGregorio et al. (1999)
EGTA (c_{4f} , c_{4c})	1.5×10^{-2}	1.06×10^{-3}	None	None	Variable	1.4×10^{-6}	Nagerl et al. (2000)
ATP (c_{5f} , c_{5c} , c_{5m})	1×10^{-1}	6	1.3×10^{-2}	3.9×10^{-1}	5000	1.4×10^{-6}	Baylor and Hollingworth (1998)
Parvalbumin (c_{6f} , c_{6c} , c_{6m})	2.5×10^{-2}	0.7	1.5×10^{-5}	3×10^{-3}	900	3.74×10^{-7}	Johnson et al. (1999); Maughan and Godt (1999)
Troponin (c_{7f} , c_{7c})	1.5×10^{-1}	4.5×10^{-1}	None	None	240	0	Baylor and Hollingworth (1998); Johnson et al. (1994)

Subscripts f , c , and m indicate the buffers' molecular species which can exist in the free, Ca^{2+} -bound, and Mg^{2+} -bound form, respectively. Some buffers do not have the m form.

TABLE 3 Diffusion-reaction equations in different positions of the myofibril

Voxel #	Equation
1 (Ca ²⁺) Z-line release	$(1 + 2U)c_{n,0}^{j+1} - 2Uc_{n,1}^{j+1} = 2Sc_{n-1,0}^j + (1 - 2S)c_{n,0}^j - 2SF \left[\left(\frac{2n+1}{2n} \right) \delta R + U\delta X \right]$ $-2Sc_{n-1,0}^{j+2} + (2S+1)c_{n,0}^{j+2} = (1 - 2U)c_{n,0}^{j+1} + 2Uc_{n,1}^{j+1} - 2SF \left[\left(\frac{2n+1}{2n} \right) \delta R + U\delta X \right]$
1 (Buffers and Mg ²⁺)	$(1 + 2U)c_{n,0}^{j+1} - 2Uc_{n,1}^{j+1} = 2Sc_{n-1,0}^j + (1 - 2S)c_{n,0}^j + W\delta T$ $-2Sc_{n-1,0}^{j+2} + (2S+1)c_{n,0}^{j+2} = (1 - 2U)c_{n,0}^{j+1} + 2Uc_{n,1}^{j+1} + W\delta T$
2	$-Uc_{n,k-1}^{j+1} + (1 + 2U)c_{n,k}^{j+1} - Uc_{n,k+1}^{j+1} = 2Sc_{n-1,k}^j + (1 - 2S)c_{n,k}^j + W\delta T$ $-2Sc_{n-1,k}^{j+2} + (2S+1)c_{n,k}^{j+2} = Uc_{n,k-1}^{j+1} + (1 - 2U)c_{n,k}^{j+1} + Uc_{n,k+1}^{j+1} + W\delta T$
3	$-2Uc_{n,m-1}^{j+1} + (1 + 2U)c_{n,m}^{j+1} = 2Sc_{n-1,m}^j + (1 - 2S)c_{n,m}^j + W\delta T$ $-2Sc_{n-1,m}^{j+2} + (2S+1)c_{n,m}^{j+2} = 2Uc_{n,m-1}^{j+1} + (1 - 2U)c_{n,m}^{j+1} + W\delta T$
4	$(1 + 2U)c_{i,0}^{j+1} - 2Uc_{i,1}^{j+1} = S \left(\frac{2i-1}{2i} \right) c_{i-1,0}^j - (2S-1)c_{i,0}^j + S \left(\frac{2i+1}{2i} \right) c_{i+1,0}^j + W\delta T$ $S \left(\frac{-2i+1}{2i} \right) c_{i-1,0}^{j+2} + (2S+1)c_{i,0}^{j+2} - S \left(\frac{2i+1}{2i} \right) c_{i+1,0}^{j+2} = (1 - 2U)c_{i,0}^{j+1} + 2Uc_{i,1}^{j+1} + W\delta T$
5	$-Uc_{i,k-1}^{j+1} + (1 + 2U)c_{i,k}^{j+1} - Uc_{i,k+1}^{j+1} = S \left(\frac{2i-1}{2i} \right) c_{i-1,k}^j + (1 - 2S)c_{i,k}^j + S \left(\frac{2i+1}{2i} \right) c_{i+1,k}^j + W\delta T$ $-S \left(\frac{2i-1}{2i} \right) c_{i-1,k}^{j+2} + (1 + 2S)c_{i,k}^{j+2} - S \left(\frac{2i+1}{2i} \right) c_{i+1,k}^{j+2} = Uc_{i-1,k}^{j+1} + (1 - 2U)c_{i,k}^{j+1} + Uc_{i,k+1}^{j+1} + W\delta T$
6	$-2Uc_{i,m-1}^{j+1} + (1 + 2U)c_{i,m}^{j+1} = S \left(\frac{2i-1}{2i} \right) c_{i-1,m}^j + (1 - 2S)c_{i,m}^j + S \left(\frac{2i+1}{2i} \right) c_{i+1,m}^j + W\delta T$ $S \left(\frac{-2i+1}{2i} \right) c_{i-1,m}^{j+2} + (2S+1)c_{i,m}^{j+2} - S \left(\frac{2i+1}{2i} \right) c_{i+1,m}^{j+2} = 2Uc_{i,m-1}^{j+1} + (1 - 2U)c_{i,m}^{j+1} + W\delta T$
7	$(1 + 2U)c_{0,0}^{j+1} - 2Uc_{0,1}^{j+1} = 4Sc_{1,0}^j + (-4S+1)c_{0,0}^j + W\delta T$ $(4S+1)c_{0,0}^{j+2} - 4Sc_{1,0}^{j+2} = 2Uc_{0,1}^{j+1} + (1 - 2U)c_{0,0}^{j+1} + W\delta T$
8	$-Uc_{0,k-1}^{j+1} + (1 + 2U)c_{0,k}^{j+1} - Uc_{0,k+1}^{j+1} = (-4S+1)c_{0,k}^j + 4Sc_{1,k}^j + W\delta T$ $(4S+1)c_{0,k}^{j+2} - 4Sc_{1,k}^{j+2} = Uc_{0,k-1}^{j+1} + (1 - 2U)c_{0,k}^{j+1} + Uc_{0,k+1}^{j+1} + W\delta T$
9	$-2Uc_{i,m-1}^{j+1} + (1 + 2U)c_{i,m}^{j+1} = 4Sc_{1,m}^j + (-4S+1)c_{0,m}^j + W\delta T$ $(4S+1)c_{0,m}^{j+2} - 4Sc_{1,m}^{j+2} = 2Uc_{i,m-1}^{j+1} + (1 - 2U)c_{i,m}^{j+1} + W\delta T$

Voxel numbers refer to Fig. 1 B. Equations and notation are derived in Appendix B. Unless indicated, equations apply to Ca²⁺, Mg²⁺, and buffers. The first and second lines for each voxel are the equations that governed the diffusion-reaction for the first and second half time-step, respectively, of the ADI method.

The second component of W_1 is the Ca²⁺-ATPase (P_1), located at the SR membrane, that pumps Ca²⁺ against its concentration gradient from the cytoplasm to the lumen of the SR (Ebashi and Endo, 1968). In the model, the SR-ATPase was located in voxels denoted by 2 and 3 in Fig. 1 B. Although it is thought that the SR-ATPase may have complex kinetics (Burmeister-Getz and Lehman, 1997), its operation was approximated by the equation:

$$P_1 = - \frac{V_{\max}}{1 + \left(\frac{K_M^{\text{SR}}}{c_1} \right)^2}, \quad (1.14)$$

where P_1 is the rate of change of [Ca²⁺] due to pumping, V_{\max} is the maximal reaction velocity, and K_M^{SR} is the Michaelis-Menten constant. The calculation of V_{\max} involves estimating the SR surface area in a typical myofibril (Table 1), which we approximated from the literature ratio of SR surface area to fiber volume (Eisenberg, 1983). Thus,

$$1.571 \mu\text{m}^3 \text{ of myofibril} \times 1.49 \frac{\mu\text{m}^2 \text{ of SR}}{\mu\text{m}^3 \text{ of fiber}} = 2.34 \mu\text{m}^2 \text{ of SR}. \quad (1.15)$$

Then, multiplying Eq. 1.15 by the estimated surface density of pump molecules, 30,000 pumps/ μm^2 of SR, (Franzini-Armstrong and Ferguson,

1985) and the pumping rate per molecule, (0.0076 Ca²⁺ ions/ms) (Vilsen and Andersen, 1992), then dividing by the volume of the peripheral ring in which the SR-ATPase resides (9.17×10^{-17} L), yields a V_{\max} of 9.74 $\mu\text{M/ms}$.

Boundary and initial conditions

The diffusion reaction equation from Eq. 1.7 was integrated to conform to the boundary conditions listed in Eq. 1.16. The model assumed that there was no net Ca²⁺ flux across the boundaries, except at the Ca²⁺ release sites. Thus,

$$\left\{ \begin{array}{l} \frac{\partial c_1}{\partial x} = 0 \quad \text{at } x = 0; \quad 0 \leq r < a; \quad t \geq 0 \\ \frac{\partial c_1}{\partial x} = 0 \quad \text{at } x = l; \quad 0 \leq r \leq a; \quad t \geq 0 \\ \frac{\partial c_1}{\partial r} = 0 \quad \text{at } r = 0; \quad 0 \leq x \leq l; \quad t \geq 0 \\ \frac{\partial c_1}{\partial r} = 0 \quad \text{at } r = a; \quad 0 < x \leq l; \quad t \geq 0 \end{array} \right\}. \quad (1.16)$$

For the Z-line release model an additional boundary condition was

$$\frac{\partial c_1}{\partial r} = \frac{\partial c_1}{\partial x} = J(t) \quad \text{at } r = a; \quad x = 0; \quad t \geq 0.$$

For the extended release model,

$$\frac{\partial c_1}{\partial r} = \frac{\partial c_1}{\partial x} = 0 \quad \text{at } r = a; \quad x = 0; \quad t \geq 0$$

but Ca^{2+} ions were released into the model at each time-step resulting in a flux described by $J(t)$ at $r = a$ and $0 < x < \delta$, where δ represents the length of the release band.

The fact that the only flux across the $r = a$ boundary occurs at the release sites implicitly assumes that the surrounding myofibrils are perfectly in register with the simulated one. This assumption is supported by experimental evidence showing that there is no di-8-ANEPPS fluorescence from the T-tubules anywhere in the sarcomere except at the Z-line (DiFranco et al., 2002; Vergara et al., 2001). The boundary conditions for Mg^{2+} and all the other buffers were identical, except that they did not have the source. Thus,

$$\left\{ \begin{array}{l} \frac{\partial c_p}{\partial x} = 0 \quad \text{at } x = 0, x = 1; \quad 0 \leq r < a; \quad t \geq 0 \\ \frac{\partial c_p}{\partial r} = 0 \quad \text{at } r = 0, r = a; \quad 0 \leq x \leq 1; \quad t \geq 0 \end{array} \right\}. \quad (1.17)$$

The initial conditions for Ca^{2+} and Mg^{2+} were set as follows:

$$\left\{ \begin{array}{l} c_1(0) = 0.1 \mu\text{M} \\ \text{for } 0 \leq x \leq l; \quad 0 \leq r \leq a \\ c_2(0) = \text{calculated according to Eq. A4} \\ \text{for } 0 \leq x \leq l; \quad 0 \leq r \leq a; \quad t \leq 0 \end{array} \right\}. \quad (1.18)$$

The initial conditions for the buffers were calculated according to Eqs. 1.8–1.10.

Integration method

Since the Crank-Nicolson integration method for parabolic partial differential equations has excellent stability and convergence and allows for relatively large time-steps (Crank, 1975), we attempted its use to solve the current model equations. However, its advantage was lost when integrating in two dimensions due to the necessity of inverting large matrices for which no efficient algorithms exist. The alternating direction implicit (ADI) (Peaceman and Rachford, 1955) method allows for large time increments without the need for inverting large two-dimensional matrices and has been used to solve diffusion-reaction models in other contexts (Chiu and Hoppensteadt, 2000; Chiu and Walkington, 1997). A complete description of the implementation of the ADI method in our specific case is given in Appendix B.

Fluorescence

As stated above, the Ca^{2+} indicator OGB-5N diffused and interacted with Ca^{2+} identically to any other buffer. Fluorescence changes were calculated in terms of $\Delta F/F$ as follows:

$$\frac{\Delta F}{F}(t) = \frac{c_{3c}(t) - c_{3c}(0)}{\frac{c_{3\text{tot}}}{F_{\text{max/min}}} + c_{3c}(0)}, \quad (1.19)$$

where $F_{\text{max/min}}$ is the fluorescence ratio between saturated and free dye, and $c_{3c}(0)$ is the Ca^{2+} -dye complex at the start of the simulation, calculated as per Eq. 1.8.

Comparison with of model predictions with experimental data

To compare $\Delta F/F$ values generated by the model with experimental data we considered that the experimental data was blurred due to the microscope objective (Agard et al., 1989; Castleman, 1979; Wilson, 1990). Thus, model

fluorescence data was blurred by convolving it with the triple Gaussian approximation of the PSF of the objective. The PSF could be calculated from confocal theory (Castleman, 1979; Wilson, 1990); however, we chose to measure it directly to take into consideration the optical properties of the specific objective used (Nikon, Fluor-100 1.3 NA).

The lateral (x - y) and axial (z) resolution were determined in vitro using 0.1- to 2.0- μm diameter fluorescently labeled latex beads (Fluorospheres, size kit #2, Molecular Probes, Eugene, OR). The beads were attached to a glass coverslip and bathed in water or embedded in 40% glucose and 0.5% agarose to mimic the refractive index of the fiber (Huxley and Niedgerke, 1958). Beads were scanned in the x - and z -directions in 100- and 500-nm steps, respectively. Fluorescence intensity as a function of position was fit to the Gaussian function,

$$F = A e^{-2\ln(r)((x-x_c)^2/\text{FWHM}^2)}, \quad (1.20)$$

where x_c is the center position, A is the amplitude and full-width at half-maximum (FWHM) is the width at $A/2$. For comparison between beads of different diameters, fluorescence values for each bead were normalized to its peak. The PSF was considered to be the normalized Cartesian triple Gaussian:

$$\text{PSF}(x, y, z) = e^{-(x^2+y^2)/2\sigma_{xy}^2} e^{-z^2/2\sigma_z^2}, \quad (1.21)$$

in which σ_{xy} and σ_z are the standard deviations of the Gaussian fits to the smallest resolvable bead. The FWHM of Gaussian fits to the fluorescence profiles of beads smaller than the diffraction limit were 0.35 and 0.75 μm in the x - and z -directions, respectively. This corresponded to a σ_{xy} of 0.21 and a σ_z of 0.45.

To convolve the Cartesian PSF with the model-generated $\Delta F/F$ profile at a given time ($\Delta F/F$ snapshot), a three-dimensional Cartesian snapshot of the fiber was generated from the cylindrical model. The convolution was performed either in the Fourier domain, using a custom-made program implementing a three-dimensional FFT algorithm (Press et al., 1996) or in the space domain using an algorithm that directly implemented a convolution (Novo and Vergara, unpublished results). Both methods yielded identical results, although the Fourier method was significantly faster. Experimentally measured bead fluorescence profiles closely approximated blurred model bead simulations (data not shown).

To compare model data with the experimentally obtained localized fluorescence transients, we took into account that in our experimental setup the detection pinhole would only accept light from a 0.5- μm disc region of the myofibril (Vergara et al., 2001; DiFranco et al., 2002). As an approximation, the simulated pinhole was considered to be a 0.5- μm square located at the $(x, y, 0)$ plane of the myofibril. To obtain the fluorescence at a particular x -position from 0–1, the square was centered at the edge of the myofibril ($y = a$), and at that x -coordinate. Blurred fluorescence values from voxels that were within the pinhole were summed to yield a fluorescence value for that x -position.

Transients were characterized by several kinetic properties (DiFranco et al., 2002):

1. The delay time (t_d , in ms) corresponds to the period between the time of stimulus delivery ($t = 0$) and the initiation of the rising phase of the transient, defined as the first moment when the fluorescence is sustained for 0.2 ms at two standard deviations (SDs) above F_{rest} . For simulations, which were noiseless, the initiation of the transient was considered to occur when the simulated $\Delta F/F$ rose two SDs above the noise of the corresponding experimental transient.
2. The rising phase of the transient was characterized by the rise time (r_t , in ms), defined as the interval between the initiation and peak of the transient.
3. The derivative at any given time point was calculated as the average slope of the lines joining the given point with the preceding and following point. The maximal derivative will be denoted $(d(\Delta F/F)/dt)_{\text{max}}$ (in ms^{-1}).

4. The peak $\Delta F/F$ ($\Delta F/F_{\text{peak}}$) is the maximum $\Delta F/F$ attained during the transient.
5. The full-duration at half-maximum (FDHM) is the length of time during which the fluorescence was greater than one-half of the $\Delta F/F_{\text{peak}}$.

RESULTS

Before we describe realistic model simulations that can be directly compared with experimental data, it is useful to examine simple Z-line release simulations to illustrate several aspects of intrasarcomeric $[\text{Ca}^{2+}]$ gradients. Fig. 2 depicts the spatial distribution of the $[\text{Ca}^{2+}]$ at the peak of an arbitrary release flux in a fiber with no buffers (Fig. 2 A) or containing 0.5 mM OGB-5N (Fig. 2, B–D). The Z-line is at longitudinal position 0 and the two M-lines symmetrically flank the Z-line at longitudinal positions $\pm 2 \mu\text{m}$. In this

model, Ca^{2+} release occurs at the outer boundary of the myofibril at the Z-line (radial position = $0.5 \mu\text{m}$). Fig. 2 A shows that at the peak of the release, the $[\text{Ca}^{2+}]$ at the release site has increased to $\sim 155 \mu\text{M}$ with a steep gradient that falls toward the M-line, where the $[\text{Ca}^{2+}]$ is $\sim 10 \mu\text{M}$. An important observation is that the gradient in the radial direction is not nearly as steep as the gradient in the longitudinal direction. The $[\text{Ca}^{2+}]$ at the center of the myofibril, $0.5 \mu\text{m}$ from the source radially, is $\sim 90 \mu\text{M}$, whereas the concentration $0.5 \mu\text{m}$ longitudinally from the source is $\sim 68 \mu\text{M}$. This phenomenon is seen irrespective of the simulation conditions and reflects a general property of the cylindrical geometry due to the fact that Ca^{2+} is being released in a ring around the myofibril and converges toward its central axis. Analytical solutions of the diffusion equation

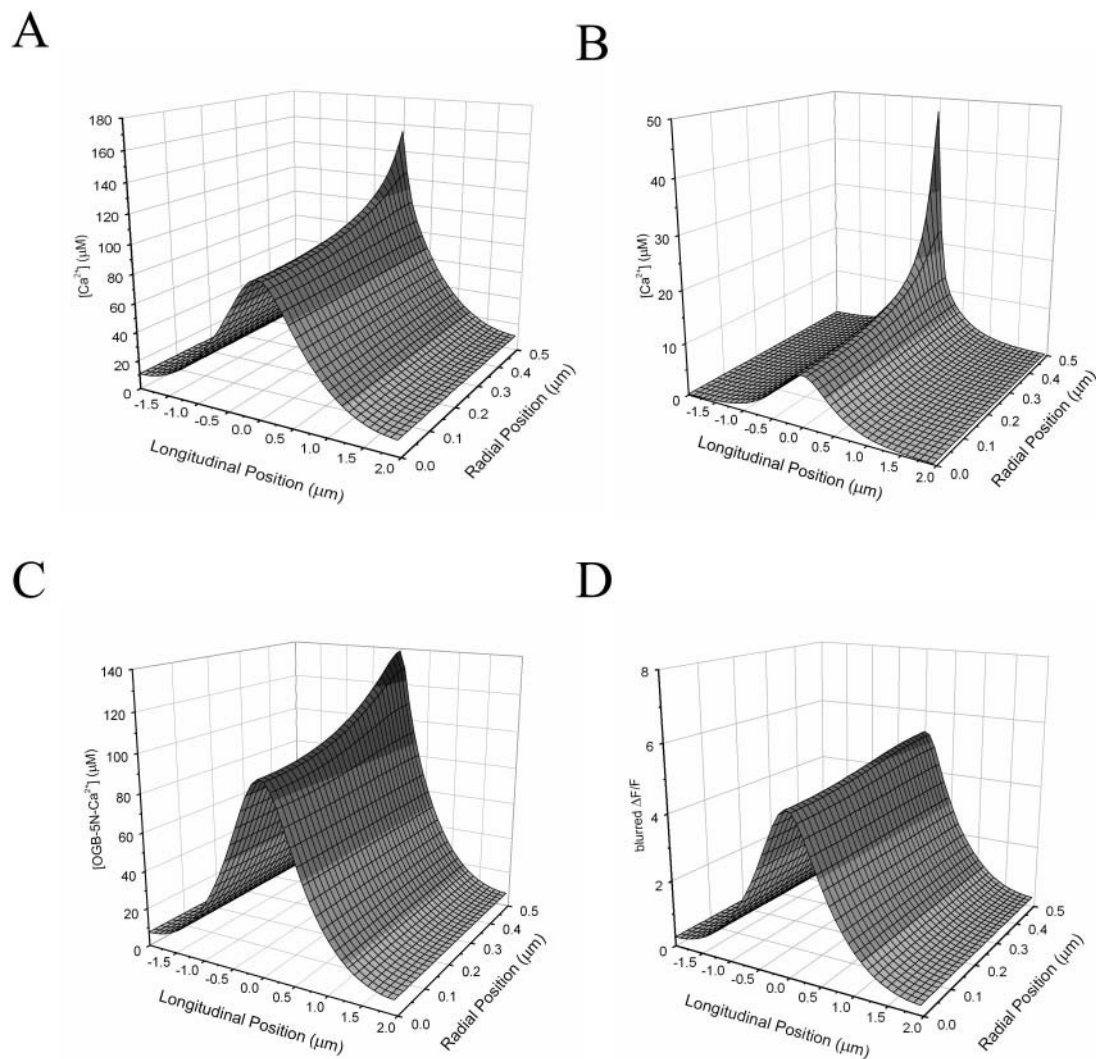


FIGURE 2 Effects of OGB-5N and microscope blurring on the fluorescence gradients. A Z-line release simulation was conducted in a standard myofibril (Table 2) with an arbitrary flux ($J_{\text{max}} = 200 \text{ pmoles}/(\text{cm}^2 \times \text{ms})$, $\tau_{\text{on}} = 4 \text{ ms}$, $\tau_{\text{off}} = 3 \text{ ms}$). (A) Spatial profile of free $[\text{Ca}^{2+}]$ at the peak of the release (2.2 ms after the initiation of Ca^{2+} release) in a myofibril devoid of buffers. (B) Spatial free $[\text{Ca}^{2+}]$ profile at the peak of the release in an identical simulation as A except that $500 \mu\text{M}$ OGB-5N was included. (C) Spatial profile of OGB-5N bound to Ca^{2+} at the peak of the release. (D) Spatial $\Delta F/F$ profile at the peak of the release blurred according to the PSF of the microscope objective.

for a point source Ca^{2+} release predict that the $[\text{Ca}^{2+}]$ in the immediate vicinity of the source is inversely proportional to the diffusion coefficient for Ca^{2+} ions (D_1) (Stern, 1992; Pape et al., 1995). In our model, the peak $[\text{Ca}^{2+}]$ in the voxel immediately adjacent to the Z-line changed from 102 to 242 μM when D_1 was changed from 4×10^{-6} to 1×10^{-6} cm^2/s , illustrating that the voxel dimension is small enough to give results that are compatible with analytical predictions.

Since we measured $[\text{Ca}^{2+}]$ with a fluorescent indicator (OGB-5N), which also acts as a mobile buffer, it is important to understand the relationship between the spatiotemporal distribution of the dye and that of free $[\text{Ca}^{2+}]$. The simulations in Fig. 2, B–D, were identical to that in Fig. 2 A, except that 0.5 mM OGB-5N was included. Fig. 2 B shows the $[\text{Ca}^{2+}]$ snapshot at the peak of the release to show how the $[\text{Ca}^{2+}]$ is modified by the presence of dye. It can be seen that the free $[\text{Ca}^{2+}]$ is decreased with respect to the case with no dye (Fig. 2 A), and that it has become more narrowly circumscribed to the release site. The fact that the Ca^{2+} -bound OGB-5N seen in Fig. 2 C is broader than the actual $[\text{Ca}^{2+}]$ profile seen in Fig. 2 B reflects the spatial filtering imposed by OGB-5N binding kinetics. The $\Delta F/F$ profile can be calculated from Fig. 2 C by the application of Eq. 1.19 and effectively normalizes the bound OGB-5N profile while preserving most of its spatial features. Fig. 2 D shows the $\Delta F/F$ profile after it was blurred by convolving it with the PSF of the microscope objective as described in Methods. Fig. 2 D clearly shows that the major effect of blurring on the $\Delta F/F$ profile is the minimization of the fluorescence gradient in the radial dimension of the myofibril. Various model simulations (data not shown) have demonstrated that this occurs because σ_z from Eq. 1.21 is significantly greater than σ_{xy} , hence serves to “mix” the high and low fluorescence regions in the radial direction more than the longitudinal direction. For example, when σ_{xy} was set equal to σ_z , the gradients in both directions were equally blurred.

Comparison of model predictions with experimental data

Whereas model simulations allow us to predict the spatiotemporal characteristics of $[\text{Ca}^{2+}]$ profiles in both the radial and longitudinal directions of the myofibril, the spot detection methodology allows only for the acquisition of fluorescence signals at various longitudinal positions of the myofibril that are blurred by the PSF of the objective. As explained above (Fig. 2 D), the major effect of blurring is that it collapses the radial dependence of the fluorescence gradients. Thus, by recording fluorescence signals from several longitudinal positions and plotting them against the distance from the Z-line at which they were acquired, we obtain the spatiotemporal profile of the “radially-averaged” $\Delta F/F$ changes in a myofibril (Ca^{2+} domain) (DiFranco et al., 2002; Vergara et al., 2001). A typical experimental domain is shown in Fig. 3 A. To allow comparison with the

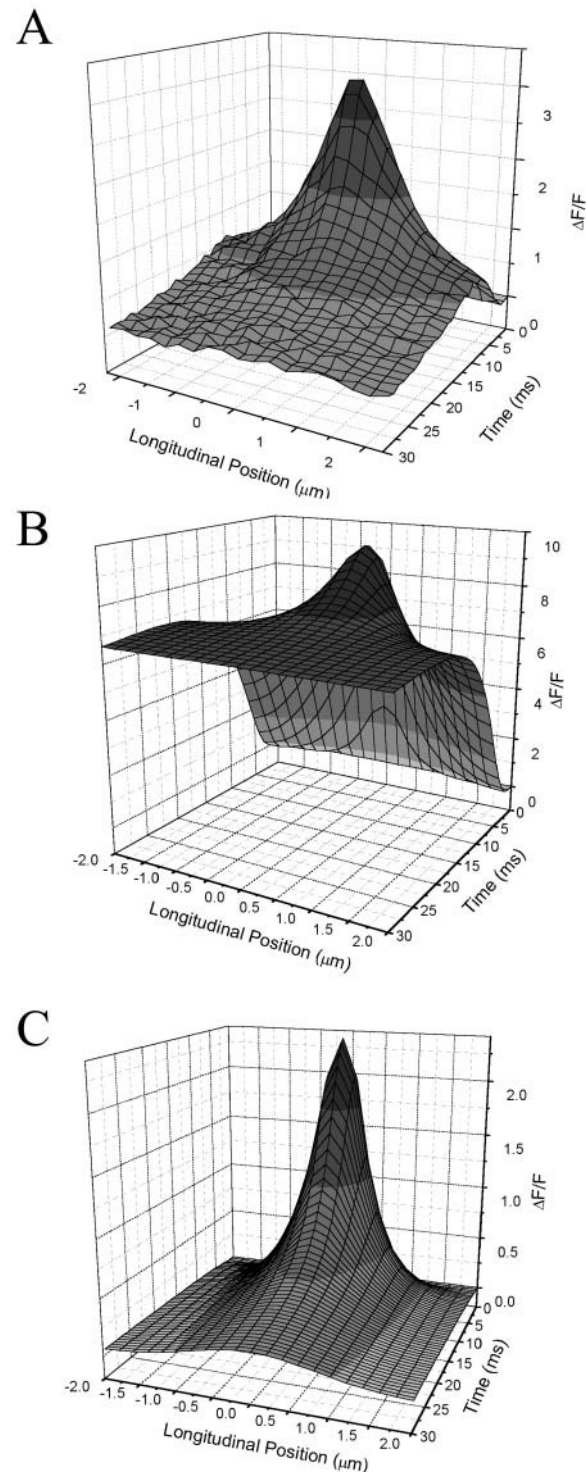


FIGURE 3 Comparison between model and experimental AP-evoked Ca^{2+} domains. (A) Experimental domain measured in a fiber equilibrated with 0.5 mM EGTA, 0.5 mM OGB-5N, 5 mM ATP, and 2 mM Mg . (B) Z-line model-simulated domain with only 0.5 mM OGB-5N and identical release flux parameters as Fig. 2. (C) Z-line model-simulated domain using the fiber conditions described in A and a release flux identical to Fig. 2. Simulation also contained parvalbumin and troponin as described in Table 2.

experimental data, model domains were constructed from simulated data as described in Methods. A $\Delta F/F$ domain from a Z-line release simulation using identical parameters as in Fig. 2, B–D, is shown in Fig. 3 B. It is possible to see that $\Delta F/F$ gradients develop early in time and that by 20 ms the gradients dissipate with an elevated fluorescence throughout the myofibril. Fig. 3 C is a domain from a model simulation using more realistic conditions. Although the release flux was identical to that used in Fig. 3 B, endogenous Ca^{2+} buffers (Table 2) and the SR-ATPase (Table 1) were included in the simulation that generated Fig. 3 C. These additions resulted in a domain that looks qualitatively similar to the experimental domain (Fig. 3 A). The fact that the $\Delta F/F$ decreased almost back to baseline values within 30 ms, and was constrained to a narrower region around the release site, is primarily due to the presence of Ca^{2+} buffers rather than the SR ATPase since removing the latter did very little to the $\Delta F/F$ domain at this timescale (data not shown). Also, once the other buffers were included, the dependence of the Ca^{2+} domain on D_1 was almost eliminated. Unlike the case with no indicator present, changing D_1 from 1×10^{-6} to 4×10^{-6} cm^2/s had a negligible effect on the peak magnitude of the Ca^{2+} domain (data not shown). This is because, in our model, most of the Ca^{2+} is rapidly bound and diffusion of the various Ca^{2+} -dye complexes becomes the primary mechanism by which Ca^{2+} redistributes within the myofibril.

The magnitude and time-course of the Ca^{2+} release flux from the SR were important unknown model parameters that required quantitative evaluation. Most other parameters had values that were either fixed by the experimental protocol (i.e., concentrations, sarcomere length, initial conditions, etc.) or obtained from the literature (Tables 1 and 2). To simulate an experimentally observed Ca^{2+} transient, the release flux was adjusted until the predicted transient at the Z-line coincided with the experimental one. According to the Z-line release model, the kinetics of the Z-line transient should be the most sensitive measure of the release kinetics because of its immediate proximity to the Ca^{2+} release site. Fig. 4 A shows an averaged experimental Z-line transient (solid line) compared with a simulated one (dashed line) from the Z-line release model. The release function used to generate the simulated transient ($J_{\text{max}} = 875$ $\text{pmoles}/(\text{cm}^2 \times \text{ms})$, $\tau_{\text{on}} = 5$ ms and $\tau_{\text{off}} = 1.6$ ms) results in a simulated transient that closely fits the experimental data (Fig. 4 A). However, this release flux did not reproduce the average experimental M-line transient (Fig. 4 B), which exhibits a larger $\Delta F/F_{\text{peak}}$, faster kinetics, and a significantly shorter delay. With the Z-line model, no matter what flux parameters we used, we could not simultaneously predict the experimental M- and Z-line transients. For example, to simulate the experimental $\Delta F/F_{\text{peak}}$ of 0.5 that is observed at the M-line, a J_{max} of 1200 $\text{pmoles}/(\text{cm}^2 \times \text{ms})$ was required, but this resulted in a simulated Z-line that greatly overestimated the amplitude of the Z-line transient (data not shown). In

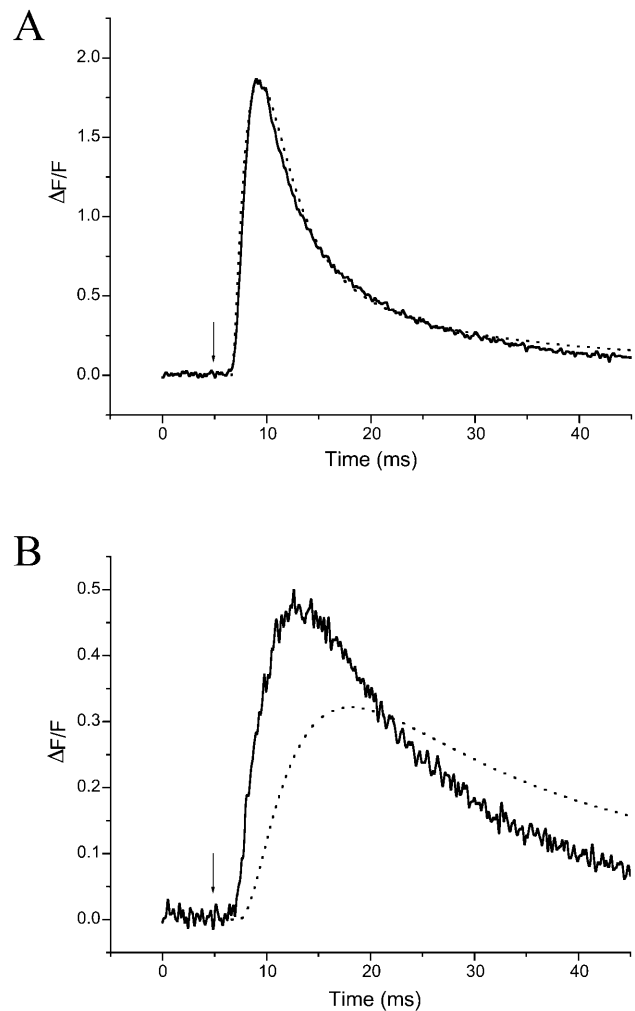


FIGURE 4 Comparison between average experimental Z- and M-line transients and Z-line model predictions. (A) The flux parameters ($J_{\text{max}} = 875$ $\text{pmoles}/(\text{cm}^2 \times \text{ms})$, $\tau_{\text{on}} = 5$ ms, and $\tau_{\text{off}} = 1.6$ ms) were adjusted such that the simulated Z-line transient (dashed lines) matched the average Z-line transient (solid line) from 32 different sarcomeres (four fibers). The fiber was stimulated at 5 ms (arrows). $\Delta F/F_{\text{peak}} = 1.88$, $rt = 2.8$ ms, $FDHM = 5.94$ ms, and $(d(\Delta F/F)/dt)_{\text{max}} = 1.3$ ms^{-1} . All simulated and experimental transients were obtained under conditions identical to Fig. 3. (B) The M-line transient (dashed line) from the same simulation as A is compared to the averaged experimental M-line transient (solid line). Properties of experimental trace: $\Delta F/F_{\text{peak}} = 0.5$, $rt = 6.3$ ms, $FDHM = 16.2$ ms, and $(d(\Delta F/F)/dt)_{\text{max}} = 0.38$ ms^{-1} . Properties of simulation trace: $\Delta F/F_{\text{peak}} = 0.32$, $rt = 8.53$ ms, $FDHM = 31.37$ ms, and $(d(\Delta F/F)/dt)_{\text{max}} = 0.063$ ms^{-1} .

addition, the predicted M-line peak occurred at 12.7 ms, much later than the 7.6-ms peak time of the experimental trace. Thus, with the buffer parameters tested so far, the difference between the experimental and simulated M-line transients cannot be accounted for by the properties of the Z-line Ca^{2+} release model.

We then examined whether varying some of the buffer parameters in Table 2 would allow us to simultaneously predict the experimental Z- and M-line transients with the same flux in Z-line model simulations. The SR Ca^{2+} flux was

adjusted such that the simulated Z-line transient matched the average experimental Z-line transient for every condition tested, as shown in Fig. 4 A. An obvious parameter that is expected to have an influence on the model predictions is the diffusion coefficient of OGB-5N (D_3). Fig. 5 A shows comparisons between the experimental M-line transients in Z-line release simulations where D_3 was varied from 1.4×10^{-6} to 9×10^{-6} cm²/s. It can be seen that when D_3 was assumed to be 3.8×10^{-6} cm²/s, then the predicted M-line transient (Fig. 5 A, dashed line trace) had an amplitude comparable to that of the experimental one (solid line trace) but failed to predict other parameters (i.e., Z–M delay, rt). When an even larger value of D_3 was used (9×10^{-6} cm²/s; dash-dot line trace, Fig. 5 A), the delay and the early part of the rising phase of the transient could be predicted, but the amplitude significantly exceeded the experimental trace.

It is well-known that the diffusion coefficient of small molecules depends on the viscosity (Hobbie, 1997) and cytoarchitecture of the intracellular milieu (Kao et al., 1993). The diffusion coefficients for fluorescent probes comparable to OGB-5N have been measured to be approximately fourfold slower in the intracellular environment than in water (Kao et al., 1993; Woods and Vergara, 2002). Since we have measured D_3 in water to be 5.6×10^{-6} cm²/s (Woods and Vergara, 2002), we consider 1.4×10^{-6} cm²/s a reasonable estimate of D_3 inside the cell, in which case the model simulated transient is very different from the experimental one (Fig. 4 B, Fig. 5 A, dotted line trace).

ATP is the most abundant Ca²⁺ buffer in our simulations and has been shown to have the potential to condition Ca²⁺ signaling within a muscle fiber (Baylor and Hollingworth, 1998). The ability of ATP to influence the simulations strongly depends on the steady-state free [ATP] (i.e., before the stimulus), which is assumed to be identical to that in the cut end pools (~3 mM) (DiFranco et al., 2002). Even with such a high free [ATP], the D_{ATP} that was required in Z-line release model simulations to come close to predicting the M-line transients was 3.8×10^{-6} cm²/s (data not shown), which is much higher than commonly assumed in the literature (Baylor and Hollingworth, 1998).

A critical parameter that can be used to compare experimental results with model simulations is the Z–M delay because it has the potential to distinguish between localized and extended Ca²⁺ release sites within the sarcomere (Hollingworth et al., 2000; Escobar et al., 1994). We have recently addressed this issue by carefully determining, under conditions that are expected to have high free [ATP], that the average Z–M delay in amphibian muscle fibers is 0.64 ± 0.1 ms (mean \pm SD, $n = 30$) (DiFranco et al., 2002). In contrast, quantitative evaluation of the Z–M delay from Z-line model simulations, using the criteria described in Methods, predicts a significantly larger value of 1.5 ms. Only improbable values for diffusion coefficients were able to approximate the kinetic features of the M- and Z-line transients and the Z–M delay. Thus, we explored the

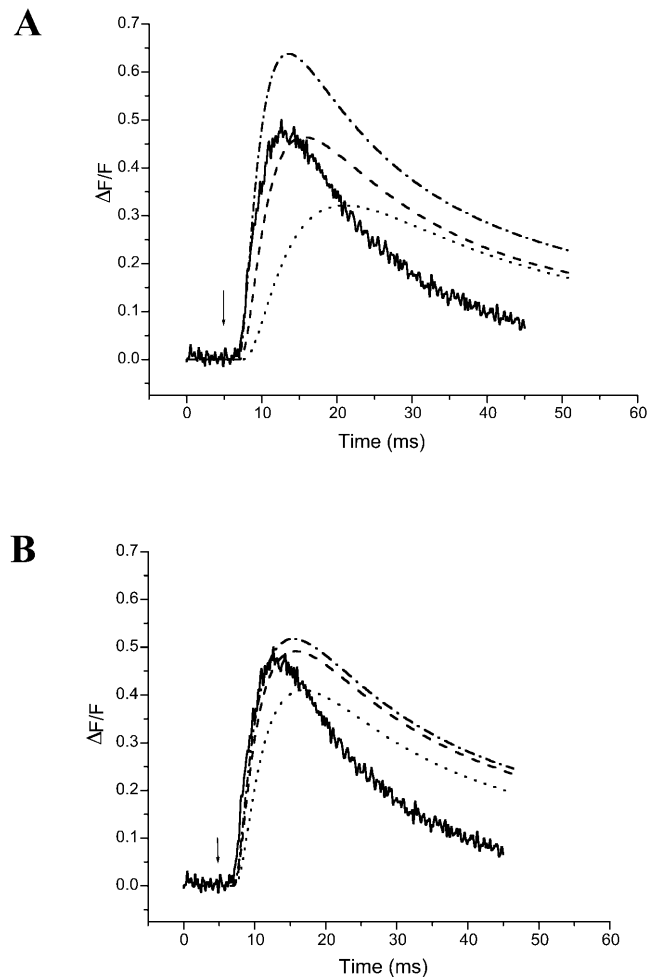


FIGURE 5 Effects of altering critical model parameters on the simulated M-line transient. The experimental AP was initiated at 5 ms (arrow). In all simulations, the flux was adjusted such that the modeled Z-line transient matched the experimental one. (A) The experimental M-line transient (thick solid line) is plotted against simulated M-line transients obtained from the Z-line release model in which D_3 was 1.4×10^{-6} (dotted line), 3.8×10^{-6} (dashed line), or 9×10^{-6} (dash-dot line) cm²/s. Modeled transient properties are in the order 1.4×10^{-6} , 3.8×10^{-6} , and 9×10^{-6} cm²/s: $rt = 12.1$, 8.32 , and 6.53 ms; $\Delta F/F_{\text{peak}} = 0.32$, 0.46 , and 0.70 ; $(d(\Delta F/F)/dt)_{\text{max}} = 0.05$, 0.11 , and 0.20 ; and $t_d = 1.81$, 1.12 , and 0.67 ms. (B) The experimental M-line transient (thick solid line) is plotted together with simulated M-line transients where the release site was extended to 0.6 (dotted line), 0.8 (dashed line), or 0.9 (dash-dot line) μm from the Z-line. The release flux was identical across the entire release band. Modeled release fluxes and transient properties are in the order 0.6 , 0.8 , and 0.9 μm . $J_{\text{max}} = 77$, 87 , and 80 pmoles/(cm² \times ms); $\tau_{\text{on}} = 5$, 5 , and 5 ms; $\tau_{\text{off}} = 1.3$, 1.1 , and 1.1 ms; $rt = 9.76$, 9.2 , and 8.6 ms; $\Delta F/F_{\text{peak}} = 0.41$, 0.49 , and 0.51 ; $(d(\Delta F/F)/dt)_{\text{max}} = 0.095$, 0.135 , and 0.15 ; and $t_d = 1$, 0.6 , and 0.6 ms.

possibility of increasing the extent of the release site while maintaining realistic diffusion coefficients. Fig. 5 B shows that M-line transients simulated using a D_3 value of 1.4×10^{-6} cm²/s, but with an extended release site, can reproduce some of the M-line features (e.g., rise time, $(d(\Delta F/F)/dt)_{\text{max}}$, Z–M delay). It can be seen that, as the extent of the release

site is increased from $0.6 \mu\text{m}$ (*dotted line*) to $0.9 \mu\text{m}$ (*dash-dot line*), the rising phase gets faster, the Z - M delay is significantly decreased, and the $\Delta F/F_{\text{peak}}$ increases, yielding a much closer approximation to the rising phase of the experimental M -line transient. As expected, the Ca^{2+} flux required to predict the Z -line transient in the extended release site model decreased as the width of the release band was increased. Some discrepancies between predicted and experimental M -line transients still remain; particularly the falling phase of the experimental M -line transient which is significantly faster than predicted by the model. Additional simulations showed that the falling phase of the M -line transient is far more dependent on the density and kinetics of the SR ATPase than the specific properties of the release sites (data not shown).

So far, we have shown that the Z -line release model cannot predict the experimentally observed localized transients with reasonable values for the critical model parameters, but that the extended release model affords much better agreement. To more directly assess the kinetics and localization of the Ca^{2+} release from the SR, we chose to record and model AP-induced Ca^{2+} transients under conditions where the myofibril was loaded with 10 or 20 mM EGTA, as described in Methods. It has been suggested theoretically that these concentrations are sufficient to constrain the free $[\text{Ca}^{2+}]$ change to the immediate vicinity of the release site (Neher, 1998; Stern, 1992; Pape et al., 1995) and effectively accelerate the kinetics of the OGB-5N transients (DiGregorio et al., 1999). In Z -line model simulations the flux parameters were adjusted such that the simulated Z -line transient reproduced the experimentally observed one in 0.5 mM EGTA (Fig. 6 A). The Z -line transient from the same fiber equilibrated with 20 mM EGTA is shown in Fig. 6 B. It should be noticed that increasing the [EGTA] caused the $\Delta F/F_{\text{peak}}$ to decrease from 1.7 to 0.65 and the full-duration at half-maximum (FDHM) to decrease from 7.4 to ~ 4.1 ms. These effects were well-predicted by the Z -line model by simply changing the [EGTA] from 0.5 mM (Fig. 6 A) to 20 mM (Fig. 6 B). Very similar results were obtained in extended model simulations.

Normalized spatial profiles of $\Delta F/F_{\text{peak}}$ signals under conditions of high [EGTA] from several fibers (*solid line*) and Z -line release simulations (*dotted line*) are shown in Fig. 6 C. These results show that the $\Delta F/F_{\text{peak}}$ decreases to 50% of its maximum value ~ 0.5 - μm away from the release site, whereas the normalized experimental $\Delta F/F_{\text{peak}}$ profile is much broader. In addition, the experimental $\Delta F/F_{\text{peak}}$ signals significantly exceed model predictions for distances $>0.2 \mu\text{m}$ away from the Z -line, both at 10 and 20 mM EGTA. Fig. 6 D illustrates that a simple way to obtain a better approximation to the experimental spatial profile is to increase the extent of the release site. By allowing uniform release to extend $0.6 \mu\text{m}$ from the Z -line (*dotted line*), the simulated $\Delta F/F_{\text{peak}}$ profile becomes comparable to the experimental one. However, by extending the release site

to distances $>0.8 \mu\text{m}$ the predicted $\Delta F/F_{\text{peak}}$ profiles become broader than the experimental one. It should be noted that in the simulations shown in Fig. 6 D, the experimental $\Delta F/F_{\text{peak}}$ remained higher than predicted at distances $>1.2 \mu\text{m}$ from the Z -line. However, the standard deviation of the experimental trace is large in this region, due to the fact that the fluorescence signals are relatively small.

DISCUSSION

In this article, we describe a three-dimensional diffusion-reaction model of a skeletal muscle myofibril that is based on the one described by Cannell and Allen (1984). Similar to Baylor and Hollingworth (1998), we have incorporated the diffusion and reaction of all relevant buffer species within the myofibril. However, we have extended their model in several ways to both improve the accuracy and convergence of the integration as well as to allow for the direct comparison of model predictions with experimental results obtained using the confocal spot detection system (Escobar et al., 1994; DiFranco et al., 2002; Vergara et al., 2001). Instead of the Euler explicit integration method used previously (Baylor and Hollingworth, 1998) we have utilized an implicit ADI method (Appendix B) that eliminates the necessity of using very small time-steps (Peaceman and Rachford, 1955; Smith, 1985), and has been successfully used to model systems of diffusion-reaction equations in other biological problems (Chiu and Walkington, 1997; Chiu and Hoppensteadt, 2000). The typical time-step required to obtain convergence in the Z -line release simulations was $4 \mu\text{s}$, although a 2 - μs time-step was required in simulations with large concentrations (>5 mM) of any free buffer. Due to their complexity, the extended release simulations required a shorter time-step of $0.2 \mu\text{s}$ to guarantee stability. These relatively large integration time-steps allowed us to divide the simulated myofibril into many more voxels than previously used (Cannell and Allen, 1984; Baylor and Hollingworth, 1998), thus increasing the accuracy of the model, although still allowing the simulation to complete in a reasonable amount of time.

Although a previous myofibril model (Baylor and Hollingworth, 1998) considered that Ca^{2+} and Mg^{2+} compete for binding to ATP, it incorporated a reaction scheme approximation that avoided an explicit calculation of the competition. However, comparison of our model predictions with and without this approximation showed that it induces an $\sim 10\%$ error in the resulting $\Delta F/F$ profiles; hence we chose to calculate the competition directly in every simulation.

In addition, several enhancements were required to compare model simulations with experimental data. Firstly, the simulated fluorescence distribution was blurred using a triple Gaussian approximation of the PSF, as determined directly for our experimental setup. Secondly, a localized transient at a single longitudinal position of the sarcomere

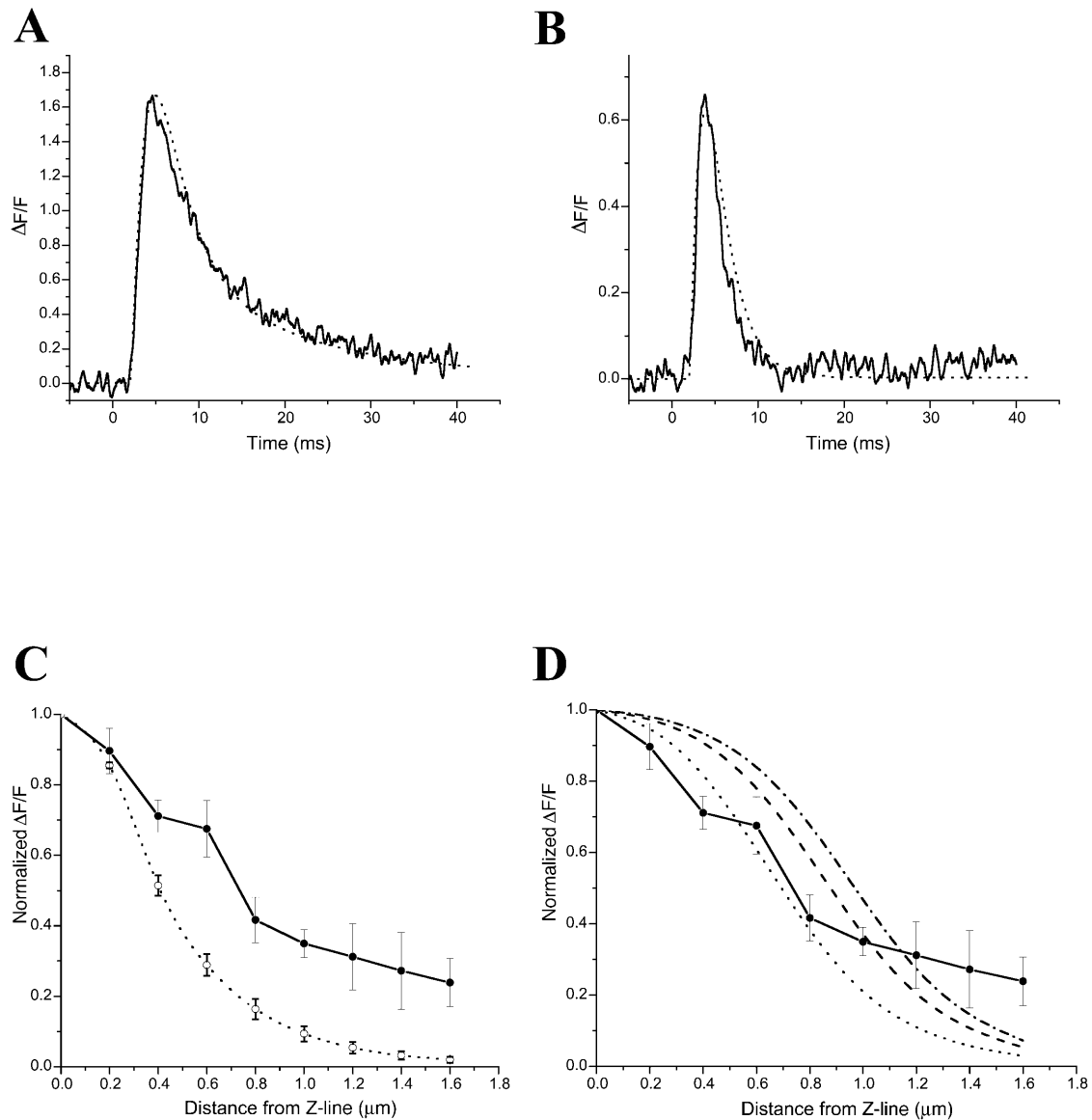


FIGURE 6 The effects of high [EGTA] on properties of the Ca^{2+} signals. (A) The experimental Z-line transient (solid line) was recorded from a fiber equilibrated with 0.5 mM EGTA. The simulated transient (dotted line) was obtained using a Z-line release model. The simulated flux parameters were adjusted ($J_{\text{max}} = 850 \text{ pmoles}/(\text{cm}^2 \times \text{ms})$, $\tau_{\text{on}} = 5.5 \text{ ms}$, and $\tau_{\text{off}} = 5.8 \text{ ms}$) until the simulated Z-line transient matched the experimental one. (B) The experimental Z-line transient (solid line) was obtained from the same fiber as A, after equilibration with 20 mM EGTA. The simulated transient (dotted line) was obtained using a Z-line release model. (C) Averaged normalized $\Delta F/F_{\text{peak}}$ values from transients recorded at different distances from the Z-line in four different fibers, two with 10 mM EGTA and two with 20 mM EGTA (solid line and circles). The simulated profile (dotted line and open circles) was obtained from transients generated using the Z-line release model. The data was normalized to the $\Delta F/F_{\text{peak}}$ at the Z-line. (D) Normalized $\Delta F/F_{\text{peak}}$ values from transients recorded at different distances from the Z-line in extended model simulations compared to experimental data. The release site was extended to 0.6 (dotted line), 0.8 (dashed line), and 0.9 (dash-dot line) μm .

was assumed to arise from a simulated detection pinhole that measures the blurred fluorescence from a square area centered in the middle z -axis plane of the myofibril. Thirdly, the simulated pinhole was moved longitudinally in 200-nm increments to construct a simulated fluorescence domain, which was compared with the experimental domains obtained from scanned data.

Since the simulated dye fluorescence was compared directly with the experimentally observed fluorescence, it

was necessary to understand how the inclusion of dye affected the model predictions. A comparison of Fig. 2, A and B, illustrates how even the low affinity dye OGB-5N can distort the simulated $[\text{Ca}^{2+}]$ profile. Increasing the affinity of the modeled indicator to that of Fluo-3 ($K_d = 0.7 \mu\text{M}$, $k_{\text{off}} = 0.175 \text{ ms}^{-1}$; Escobar et al., 1997), while maintaining the same $F_{\text{max/min}}$ of OGB-5N, caused the $\Delta F/F_{\text{peak}}$ to decrease by 69% and resulted in much shallower gradients, both radially and longitudinally (data not shown), than those illustrated in Fig.

2D. This reinforces the idea that using a low affinity indicator affords the minimum distortion, both spatially and temporally, of the underlying Ca^{2+} gradients. Even with a low affinity indicator, the bound dye profile (Fig. 2C) is a distorted representation of the free $[\text{Ca}^{2+}]$ in the myofibril, which highlights the fact that equilibrium assumptions are invalid for rapidly changing Ca^{2+} fluxes. However, closer inspection reveals that the majority of the distortion occurs within 100 nm of the release site. The shallower gradients that exist farther from the release site are relatively undistorted by OGB-5N (e.g., compare the longitudinal gradients at the 0 radial position in Fig. 2, A and C).

The fact that the [OGB-5N- Ca^{2+}] profile in Fig. 2C looks similar to the real $[\text{Ca}^{2+}]$ profile in Fig. 2A is coincidental, due to the fact that there are no other buffers present. There is generally no simple relationship between the fluorescence profile (reporting the concentration of OGB-5N- Ca^{2+} complex) and the $[\text{Ca}^{2+}]$ that would have occurred in the absence of the dye. Thus, to fully understand the rapid evolution of the Ca^{2+} profile, it is necessary to combine high resolution measurements with computer modeling.

The blurring due to the PSF of the microscope objective introduces a further distortion of the Ca^{2+} signal. However, this effect is mainly noticeable in the radial, as opposed to the longitudinal, direction of the myofibril (Fig. 2D). Thus, the longitudinal $\Delta F/F$ gradients observed after blurring are relatively accurate representations of the true $\Delta F/F$ gradients. However, we did introduce blurring in all of our simulations because it does cause distortion at early time points when the gradients are steep even in the longitudinal direction and blurred transients are more representative of the data obtained with the confocal spot detection system.

A convenient way to visualize the spatiotemporal profile of the Ca^{2+} signal is by constructing a three-dimensional plot representing the Ca^{2+} domain (Chad and Eckert, 1984; DiFranco et al., 2002; Neher, 1998). It is interesting that a domain that is qualitatively similar to an experimental one (see Fig. 3A; see also Vergara et al., 2001; DiFranco et al., 2002) can be approximately predicted from a Z-line release model simulation that simply includes the appropriate Ca^{2+} buffers (Table 2, Fig. 3C) and does not require the SR Ca^{2+} -ATPase. A model of the Ca^{2+} signaling in presynaptic nerve terminals, which does not contain Ca^{2+} extrusion mechanisms, also predicts that the formation of domains around Ca^{2+} entry sites only requires the presence of Ca^{2+} buffers (DiGregorio et al., 1999). The minimal influence of the SR pump in our myofibrillar cylindrical model may be thought of as surprising, considering that we used higher values for V_{\max} than previously suggested (Cannell and Allen, 1984), and results from its localization to the outermost of the 32 radial shells of a 0.5- μm radius myofibril. The outer shell's volume is 6.2% of the total myofibrillar volume, which is comparable to the 5% value calculated based upon electron microscopy stereological measurements (Mobley and Eisenberg, 1975). Models in which the SR pump is present in a larger

proportion of the myofibrillar volume (Hollingworth et al., 2000; Baylor and Hollingworth, 1998) probably overestimate the volume from which the SR pump removes Ca^{2+} and therefore its contribution in shaping the Ca^{2+} transients.

Our model provides the first estimate of the Ca^{2+} release flux that is required to generate the $\Delta F/F_{\text{peak}}$ values and kinetic properties observed in localized AP-induced experimental transients. As demonstrated in Fig. 4A, a J_{\max} of 875 $\text{pmoles}/(\text{cm}^2 \times \text{ms})$ was required to predict the average experimental Z-line transient. Given the kinetics of the release function, the peak flux actually attained was 89 $\text{pmoles}/(\text{cm}^2 \times \text{ms})$. This value corresponds to a total Ca^{2+} current of 16.4 pA per AP and results in a rate of $[\text{Ca}^{2+}]$ change of 55.5 $\mu\text{M}/\text{ms}$ for a myofibril with a 0.5- μm radius and a 4- μm length. This value is ~ 2.6 -fold smaller than a previous estimate for amphibian muscle fibers based upon global Ca^{2+} measurements (Pape et al., 1995). These values are surprisingly similar, given the widely different experimental protocols and Ca^{2+} detection techniques methodologies. Based on comparisons of experimentally measured Ca^{2+} sparks (obtained with techniques more similar to those described in this article) with model predictions, Rios et al. (1999) calculated that sparks result from an ~ 8 pA current. This would suggest that Ca^{2+} sparks represent the spontaneous activation of $\sim 50\%$ of the total Ca^{2+} release flux that occurs in response to an AP during skeletal muscle EC coupling, seemingly too large for their proposed role as the elemental process underlying EC coupling in skeletal muscle (Klein et al., 1999; Rios et al., 1999).

Our model is sensitive to the free [ATP] since it is present in high concentrations and acts as a rapidly diffusing, low affinity Ca^{2+} buffer that carries Ca^{2+} throughout the myofibril (Baylor and Hollingworth, 1998). It should be noted that none of the parameters pertaining to ATP- Ca^{2+} interaction (i.e., $\text{ATP-}k_{\text{on}}$, $\text{ATP-}k_{\text{off}}$, D_{ATP}) have been measured directly inside the muscle fiber and the literature values that we chose are the ones that would generate the most rapid spread of Ca^{2+} throughout the myofibril. Moreover, since we assumed that the [ATP] and $[\text{Mg}^{2+}]$ inside the muscle fiber were initially equal to their concentrations in the cut end pools, the free [ATP] inside the myofibril was calculated to be ~ 3 mM, which is much higher than typically assumed in other models (Hollingworth et al., 2000; Baylor and Hollingworth, 1998). Also, the value for D_3 of 1.4×10^{-6} cm^2/s used in the simulations is also fast compared to the value used for other indicators in the literature (Baylor and Hollingworth, 1998; Timmerman and Ashley, 1986; Harkins et al., 1993). Despite using the fastest reasonable diffusion parameter values, the Z-line release model could not simultaneously predict the kinetic features of the experimental M- and Z-line transients, including the Z-M delay (Fig. 4). We believe that the true values for the ATP and OGB-5N properties, as determined in vivo, will be slower than the values used in our simulations, and will only increase

the discrepancies between the model predictions and the experimental data.

The Z - M delay provides a very sensitive measure of the diffusional distance from the closest Ca^{2+} release site to the M -line with minimum contamination from the kinetics of the Ca^{2+} release flux itself. Thus, the fact that the Z -line release model predicts a Z - M delay of 1.5 ms, as compared to the experimental one of 0.64 ms, is highly significant. Interestingly, simulations of extended release sites $>0.6 \mu\text{m}$ per half-sarcomere have a Z - M delay comparable to the experimental data (Fig. 5 *B*). However, simply extending the release site does not allow us to predict the entire M -line transient, and discrepancies remain in the falling phase. We tapered the amplitude of the release flux as it approached the M -line in an attempt to simultaneously predict the rising and falling phases of the experimental M -line transient. As expected, the falling phase was better predicted, but at the expense of the kinetics of the rising phase and $\Delta F/F_{\text{peak}}$ (data not shown). Further modeling showed that the rising phase of the M -line transient was mostly sensitive to the extent and kinetics of the release flux while the falling phase was primarily affected by the density and kinetics of the SR ATPase in the vicinity of the M -line. By changing the density of the SR pump and ascribing to it an arbitrary delayed activation kinetics, similar to those used by Baylor and Hollingworth (1998), we were able to predict the entire M -line transient (data not shown). Further studies designed to probe the kinetics of Ca^{2+} removal from the myofibril are required to explain the complete Ca^{2+} release and reuptake process. However, it is apparent that a homogenous extended release model, which is merely a simple approximation for extended release, comes closer to predicting the rising phase and peak of the M -line transient than a point source release does.

Hollingworth et al. (2000) reported that one of their models was able to predict the short Z - M delays (~ 1 ms) that they observed using a scanning confocal microscope for fibers with a sarcomere length (SL) of $3.2 \mu\text{m}$. Our Z -line release model would also predict a comparable Z - M delay for a fiber stretched to that length, which is not surprising considering that the diffusion coefficients for buffers in our model are comparable to the fast diffusion coefficients in their *Model 2* (Hollingworth et al., 2000). Nevertheless, the experimental records that we attempted to predict were obtained from fibers stretched to a significantly longer SL of $4 \mu\text{m}$. We found that SLs of $\sim 4 \mu\text{m}$ were the maximal that afforded the intact preservation of the fiber's electrical properties and their ability to elicit transients with $\Delta F/F_{\text{peak}}$ values similar to those from less stretched fibers (data not shown). The importance of stretching the fibers is that this procedure allowed us to obtain a more accurate estimate of the spatial dependence of the signals since it minimizes the effects of blurring caused by the PSF of the microscope as compared to the overall SL, while completely abolishing movement artifacts (DiFranco et al., 2002). These are key requirements for the comparison between model predictions

and experimental data. In the presence of movement, the Ca^{2+} release sites would be coming closer together in response to the increased $[\text{Ca}^{2+}]$ and would require a much more complicated moving boundary model to compare with the experimental data (Crank, 1975). In addition, the model predicts that the Z - M delay increases very steeply with increased SL (Novo et al., 2002) and therefore longer SLs allow for improved comparison between model and experiment. Despite the longer SL, we have measured a significantly shorter Z - M delay (0.64 ± 0.1 vs. ~ 1 ms) (Vergara et al., 2001; DiFranco et al., 2002), which cannot be predicted by the Z -line release model.

To restrict the free Ca^{2+} to regions near the release sites, we recorded AP-induced fluorescence transients in the presence of 10 or 20 mM EGTA, which limited significant free $[\text{Ca}^{2+}]$ changes to within 50 nm of the Z -line (data not shown). This is in reasonable agreement with theoretical calculations of the Ca^{2+} profile around the mouth of a single Ca^{2+} channel in the presence of high EGTA (Stern, 1992; Naraghi and Neher, 1997; Pape et al., 1995, 1998). The Z -line release model was able to accurately predict the kinetics of the Z -line transient under conditions of 20 mM EGTA, using identical Ca^{2+} release flux parameters as were required to predict the Z -line transient with 0.5 mM EGTA (Fig. 6, *A* and *B*). The fact that the same flux could predict the time-course of the experimental Z -line transients in both the low and high [EGTA] attests to the capability of the model in predicting the effects of buffer competition in the neighborhood of the release site. Both the Z -line and extended release site simulations demonstrate that with >10 mM EGTA, the kinetics of the Z -line transient closely approximate underlying Ca^{2+} release flux (data not shown), suggesting that the flux parameters used in the simulations are similar to the flux parameters in the fiber under our experimental conditions.

Even though the Z -line release model can accurately reproduce the Z -line transient under conditions of high [EGTA], it predicts AP-evoked Ca^{2+} domains that are significantly narrower than seen in the experimental data (Fig. 6 *C*). At every position farther than 200 nm from the Z -line, the model predicts lower $\Delta F/F_{\text{peak}}$ values than what is observed experimentally. When the release site is extended to between 0.6 and $0.8 \mu\text{m}$, the simulated $\Delta F/F_{\text{peak}}$ fluorescence profiles predicts the experimental one more closely (Fig. 6 *D*). This observation reinforces the idea that the assumption of Ca^{2+} release occurring exclusively at the Z -line may not be accurate. The suggestion that, at distances farther than $1.2 \mu\text{m}$ from the Z -line, the experimental data exhibits a consistently higher $\Delta F/F_{\text{peak}}$ than even a $0.9\text{-}\mu\text{m}$ extended release site would predict, is intriguing but requires further experimentation due to the relatively large standard deviation of the data. It is compatible with the possibility that there may be Ca^{2+} release sites throughout the entire length of the sarcomere.

The data and model results presented in this article are compatible with the hypothesis that the initiation of the Ca^{2+}

release process occurs at the Z-line; however, modifications to a Z-line release model are required if it is to predict all of our experimental observations. There are two possible types of modifications that can cause Ca^{2+} to spread faster throughout the myofibril. The first one invokes passive mechanisms, such as increasing diffusion coefficients and kinetic parameters of Ca^{2+} and mobile buffers species, while maintaining the restricted release site assumption. As explained above, we have explored this possibility and believe that the model parameters in Table 2 are the fastest reasonable values. The second option is to abandon the Z-line release constraint and invoke the existence of active Ca^{2+} release processes from sites not exclusively located at the Z-line. This possibility is supported by the fact that simulations with extended release sites come closer to simultaneously predicting Z-line, M-line transients (rising phase, $\Delta F/F_{\text{peak}}$) and Z-M delay. It is conceivable that a broad band of release can arise from direct interactions among ryanodine receptors, as proposed by Marx et al. (1998) and/or a Ca^{2+} -induced Ca^{2+} release mechanism (Endo et al., 1970; Fabiato and Fabiato, 1975). Both of these mechanisms could account for a more rapid spread than diffusion alone (Wagner and Keizer, 1994; Sneyd et al., 1995) and are supported by reports of the existence of extrajunctional ryanodine receptors of unknown function (Dulhunty et al., 1992; Felder and Franzini-Armstrong, 2002).

A myofibrillar extended release site model, similar to ours, was recently proposed to simulate Ca^{2+} sparks in skinned mammalian muscle fibers (Uttenweiler et al., 2002). However, the range of FWHMs of their simulated domains are significantly wider (>twofold) than ours, making direct comparisons between their results and ours problematic. Further modeling in conjunction with experiments specifically designed to distinguish between release fluxes in different regions of the sarcomere would be required before a definitive explanation of the Ca^{2+} release process in skeletal muscle can be obtained.

APPENDIX A

This Appendix derives the initial free $[\text{Mg}^{2+}]$ when there is a known concentration of total buffer, total $[\text{Mg}^{2+}]$, and free $[\text{Ca}^{2+}]$.

Definition of terms

B_{tot} = total concentration of buffer B
 c_{Bf} = concentration of free buffer B
 c_{Bc} = concentration of buffer B bound to Ca^{2+}
 c_{Bm} = concentration of buffer B bound to Mg^{2+}
 K_{c}^{B} = Ca^{2+} dissociation constant of buffer B
 K_{m}^{B} = Mg^{2+} dissociation constant of buffer B
 c_1 = free Ca^{2+} concentration
 c_2 = free Mg^{2+} concentration
 $c_{2\text{tot}}$ = total Mg^{2+} concentration

Remembering that if buffer B is the only one that binds Mg^{2+} ,

$$c_{2\text{tot}} = c_{\text{Bm}} + c_2, \quad (\text{A1})$$

and combining that with Eq. 1.9, yields

$$c_{2\text{tot}} = \frac{c_2 B_{\text{tot}} (K_{\text{c}}^{\text{B}} + c_1) - c_1 c_2 B_{\text{tot}}}{(K_{\text{m}}^{\text{B}} + c_2)(K_{\text{c}}^{\text{B}} + c_1) - c_1 c_2}, \quad (\text{A2})$$

which, after rearranging, results in the quadratic equation

$$c_2^2 K_{\text{c}}^{\text{B}} + c_2 (K_{\text{m}}^{\text{B}} K_{\text{c}}^{\text{B}} + c_1 K_{\text{m}}^{\text{B}} + B_{\text{tot}} K_{\text{c}}^{\text{B}} - c_{2\text{tot}} K_{\text{c}}^{\text{B}}) - c_{2\text{tot}} K_{\text{m}}^{\text{B}} (K_{\text{c}}^{\text{B}} + c_1) = 0, \quad (\text{A3})$$

then the only valid root of Eq. A3 is

$$c_2 = \frac{-b + \sqrt{b^2 - 4ac}}{2a}, \quad (\text{A4})$$

where

$$\begin{aligned} a &= K_{\text{c}}^{\text{B}}; \\ b &= K_{\text{m}}^{\text{B}} K_{\text{c}}^{\text{B}} + c_1 K_{\text{m}}^{\text{B}} + B_{\text{tot}} K_{\text{c}}^{\text{B}} - c_{2\text{tot}} K_{\text{c}}^{\text{B}}; \\ c &= c_{2\text{tot}} K_{\text{m}}^{\text{B}} (K_{\text{c}}^{\text{B}} + c_1). \end{aligned} \quad (\text{A5})$$

APPENDIX B

This Appendix describes how cylindrical diffusion equations were solved with the ADI method. Since all diffusing species follow equations of the same general form as Eq. 1.7, we present a here a generic solution for a molecule c (instead of c_p), but distinguishing between Ca^{2+} and other buffers in setting the appropriate boundary conditions. Thus, in the notation of this Appendix, Eq. 1.7 becomes:

$$\frac{\partial c}{\partial T} = \frac{1}{R} \frac{\partial c}{\partial R} + \frac{\partial^2 c}{\partial R^2} + \frac{\partial^2 c}{\partial X^2} + W. \quad (\text{B1})$$

To derive the finite difference representation for Eq. B1, we use Taylor's series to obtain the following two equations:

$$c_{i+1,k}^j = c_{i,k}^j + \delta R \left(\frac{\partial c}{\partial R} \right) + \frac{1}{2} (\delta R)^2 \left(\frac{\partial^2 c}{\partial R^2} \right) + \dots \quad (\text{B2})$$

$$c_{i-1,k}^j = c_{i,k}^j - \delta R \left(\frac{\partial c}{\partial R} \right) + \frac{1}{2} (\delta R)^2 \left(\frac{\partial^2 c}{\partial R^2} \right) - \dots \quad (\text{B3})$$

Subtracting B3 from B2 yields a finite difference approximation for $\partial c / \partial R$ and adding B2 and B3 results in an approximation for $\partial^2 c / \partial R^2$. A similar expansion gives an approximation for $\partial^2 c / \partial X^2$. The time derivative can be replaced by its forward difference approximation to result in the following finite difference approximation for Eq. B1 (see Crank, 1975).

$$\begin{aligned} \frac{c_{i,k}^{j+1} - c_{i,k}^j}{\delta T} &= \frac{(2i+1)c_{i+1,k}^j - 4c_{i,k}^j + (2i-1)c_{i-1,k}^j}{2i(\delta R)^2} \\ &+ \frac{c_{i,k+1}^j - 2c_{i,k}^j + c_{i,k-1}^j}{(\delta X)^2} + W. \end{aligned} \quad (\text{B4})$$

Integration of Eq. B4 based on explicit methods is impractical because convergence requires an extremely small time-step (Smith, 1985; Crank, 1975; Camahan et al., 1969; Press et al., 1996). The commonly used Crank-Nicolson approximation to derive an implicit formulation from Eq. B4 is also impractical since the radial and axial directions would have to be

incremented simultaneously, involving an inversion of an $m \times n$ matrix at every time-step, which is a computationally expensive process (Smith, 1985; Crank, 1975; Carnahan et al., 1969).

The ADI provides an alternative implicit method to solve this type of problems (Peaceman and Rachford, 1955). When applied to our specific cylindrical problem, δT is divided into two half time-steps; in the first, the radial dimension is incremented, and the longitudinal dimension is incremented in the second. The advantage of this approach is that each half time-step leads to a set of equations that can be solved by the inversion of a simple tridiagonal matrix, for which an efficient Gaussian elimination algorithm exists (Carnahan et al., 1969).

Adopting the convention that $\delta T/2\delta R^2 = S$ and $\delta T/2\delta X^2 = U$, Eq. B4 becomes:

$$c_{i,k}^{j+1} - c_{i,k}^j = S \left(\frac{(2i+1)c_{i+1,k}^j - 4ic_{i,k}^j + (2i-1)c_{i-1,k}^j}{2i} \right) + U(c_{i,k+1}^{j+1} - 2c_{i,k}^{j+1} + c_{i,k-1}^{j+1}) + W\delta T \quad (\text{B5})$$

for the first half time-step, and

$$c_{i,k}^{j+2} - c_{i,k}^{j+1} = S \left(\frac{(2i+1)c_{i+1,k}^{j+2} - 4ic_{i,k}^{j+2} + (2i-1)c_{i-1,k}^{j+2}}{2i} \right) + U(c_{i,k+1}^{j+1} - 2c_{i,k}^{j+1} + c_{i,k-1}^{j+1}) + W\delta T \quad (\text{B6})$$

for the second half time-step. Moving all the $j+1$ terms in Eq. B5 and all the $j+2$ terms in Eq. B6 to the LHS yields the two primary equations

$$-Uc_{i,k-1}^{j+1} + (1+2U)c_{i,k}^{j+1} - Uc_{i,k+1}^{j+1} = S \left(\frac{2i-1}{2i} \right) c_{i-1,k}^j + (1-2S)c_{i,k}^j + S \left(\frac{2i+1}{2i} \right) c_{i+1,k}^j + W\delta T \quad (\text{B7})$$

and

$$-S \left(\frac{2i-1}{2i} \right) c_{i-1,k}^{j+2} + (1+2S)c_{i,k}^{j+2} - S \left(\frac{2i+1}{2i} \right) c_{i+1,k}^{j+2} = Uc_{i,k-1}^{j+1} + (1-2U)c_{i,k}^{j+1} + Uc_{i,k+1}^{j+1} + W\delta T. \quad (\text{B8})$$

It should be noted that $c_{i,k}^{j+1}$, the concentration at the first half time-step, is an intermediate value with no physical relevance, but that $c_{i,k}^{j+2}$ represents the true solution at the “next” time point.

General boundary conditions. We will describe first the finite difference representation of the boundary conditions shown in Eq. 1.16, and later the final equations for the two ADI half time-steps as they were implemented in the computer simulation.

a) $i = 0$: For this condition, we used the following finite difference approximation (Crank, 1975) (Smith, 1985):

$$\frac{1}{R} \frac{\partial c}{\partial R} + \frac{\partial^2 c}{\partial R^2} = \frac{4(c_{i,k}^j - c_{0,k}^j)}{(\partial R)^2}. \quad (\text{B9})$$

b) $i = i$: $c_{i+1,k}^j = c_{i-1,k}^j$.

c) $k = 0$: $c_{i,-1}^j = c_{i,1}^j$.

d) $k = m$: $c_{i,m+1}^j = c_{i,m-1}^j$.

Thus, for $i = 0$, Eq. B7 becomes

$$c_{0,k}^{j+1} - c_{0,k}^j = 4S(c_{1,k}^j - c_{0,k}^j) + U(c_{0,k-1}^{j+1} - 2c_{0,k}^{j+1} + c_{0,k+1}^{j+1}) + W\delta T \quad (\text{B10})$$

and Eq. B8 becomes

$$(4S+1)c_{0,k}^{j+2} - 4Sc_{1,k}^{j+2} = Uc_{0,k-1}^{j+1} + (1-2U)c_{0,k}^{j+1} + Uc_{0,k+1}^{j+1} + W\delta T. \quad (\text{B11})$$

Ca²⁺ boundary conditions for the Z-line release model. The boundary at $i = 0, k = 0$ must take into account that this is the position where the Ca²⁺ is entering the muscle fiber from the SR.

Ficks law, expressed in our coordinate system in normalized variables, is:

$$\frac{\partial c}{\partial X} = \frac{a\Phi}{D}, \quad (\text{B12})$$

where a is the fiber radius, Φ is the flux, and D is the diffusion coefficient. Using logic analogous to that used to obtain Eq. B4, the finite difference form of Eq. B12 becomes

$$\frac{c_{i,k+1} - c_{i,k-1}}{2\delta X} = \frac{a\Phi}{D}. \quad (\text{B13})$$

Thus

$$c_{i,-1} = c_{i,1} + \frac{a\Phi(2\delta X)}{D}, \quad (\text{B14})$$

and analogously

$$c_{-1,k} = c_{i,k} + \frac{a\Phi(2\delta R)}{D}. \quad (\text{B15})$$

Ca²⁺ boundary conditions for the extended release flux model are described in the text.

APPENDIX C

In this Appendix we describe schemes used to confirm the validity of model simulations under simple, well-understood conditions.

The Ca²⁺ release flux function delivers the correct number of ions/ms. A 1 ms, 300 pmoles/(cm² × ms) pulse released at voxel 1 (see Fig. 1) should result in an increase of 177,362 Ca²⁺ ions per ms for a fiber of typical dimensions (see Table 1). When the total number of ions in the simulation were summed under these conditions, it was found that there was an increase of 182,986 Ca²⁺ ions per ms (3% error), and the total number of Ca²⁺ ions in the myofibril remained constant after the pulse ended. We have similarly validated the extended release model and find that the actual increase in the number of ions is also within 3% of the theoretical value.

The SR pump removes the correct number of ions/ms. To test the operation of the SR pump, a simulation was conducted in which there was no Ca²⁺ release, and the initial [Ca²⁺] was set to 100 μM to saturate the pump. With an arbitrary V_{max} of 10 μM/ms, theoretical calculations indicate that there should be a decrease of 582 Ca²⁺ ions/ms. The actual decrease was found to be 600 ions/ms (3% error).

Ca²⁺ binding and unbinding to buffers in the model agree with single compartment kinetic predictions. At the start of the simulation the free [Ca²⁺] in the myofibril was set to 0, and equal concentrations (0.5 mM) of EGTA and OGB-5N were present. After a 1-ms baseline, the free [Ca²⁺] at every place in the myofibril was abruptly stepped to 5 μM and the model was allowed to proceed normally. The time-course of Ca²⁺ binding to each of the buffers was compared to predictions from a single compartment simulation integrated using a fourth-order Runge-Kutta algorithm (Berkeley Madonna, Berkeley, CA). For slow buffers (e.g., EGTA), there is <0.1% discrepancy between the two simulations. For fast buffers (e.g., OGB-5N) there was a maximum of 10% discrepancy in the predicted time-course, which subsided within 1 ms after the step was applied. This discrepancy can be attributed to the fact that our model uses a simple Euler integration to evaluate the kinetic reaction of Ca²⁺ and buffers.

Theoretical predictions of steady-state gradients in the presence of EGTA agree with model simulations. The analytical solution of the $[Ca^{2+}]$ profile in the presence of large concentrations of EGTA (Eq. D7 of Pape et al., 1995) was used to compare with our model predictions. This steady-state solution incorporates the diffusion coefficients of Ca^{2+} and EGTA as well as the magnitude of the Ca^{2+} release flux and the [EGTA]. A Z-line release simulation of a constant $5 p_{moles}/(cm^2 \times ms)$ flux in the presence of 20 mM EGTA was performed and the steady-state $[Ca^{2+}]$ profile was compared to the analytical solution. They were in agreement to within 2%. This validation indicates that both the buffers and Ca^{2+} , as well as the interaction of buffers with Ca^{2+} , are behaving as expected.

Conclusion. The small discrepancies between the actual and theoretical predictions above fall in the error range expected, due to the discretization errors in the ADI method (Smith, 1985).

The authors thank Dr. Jonathan Monck and Mr. Christopher E. Woods for helpful comments on the manuscript, and Ms. Hillary Protas for discussions on the numerical methods used.

This work was supported by National Institutes of Health grant AR25201 to J.V., Foudo Nacional de Ciencia, Tecnologia e Innovacion grant S1-2001-000-805, Venezuela, to M.D., and National Science and Engineering Research Council fellowship PGSB-242387-2001, Canada, to D.N. M.D. is a visiting professor from the Universidad Central de Venezuela.

REFERENCES

- Agard, D. A., Y. Hiraoka, P. Shaw, and J. W. Sedat. 1989. Fluorescence microscopy in three dimensions. *Methods Cell Biol.* 30:353–377.
- Baylor, S. M., and S. Hollingworth. 1998. Model of sarcomeric Ca^{2+} movements, including ATP Ca^{2+} binding and diffusion, during activation of frog skeletal muscle. *J. Gen. Physiol.* 112:297–316.
- Burmeister-Getz, E. E., and S. L. Lehman. 1997. Calcium removal kinetics of the sarcoplasmic reticulum ATPase in skeletal muscle. *Am. J. Physiol.* 272:C1087–C1098.
- Cannell, M. B., and D. G. Allen. 1984. Model of calcium movements during activation in the sarcomere of frog skeletal muscle. *Biophys. J.* 45:913–925.
- Carnahan, B., H. A. Luther, and J. O. Wilkes. 1969. Applied Numerical Methods. Wiley, New York.
- Castleman, K. 1979. Digital Image Processing. Prentice Hall, New York.
- Chad, J. E., and R. Eckert. 1984. Calcium domains associated with individual channels can account for anomalous voltage relations of Ca-dependent responses. *Biophys. J.* 45:993–999.
- Chiu, C., and F. Hoppensteadt. 2000. Mathematical models and simulations of bacterial growth and chemotaxis in a diffusion gradient chamber. *J. Math. Biol.* 42:120–144.
- Chiu, C., and N. Walkington. 1997. An ADI method of hysteretic reaction-diffusion systems. *Siam. J. Numer. Anal.* 34:1185–1206.
- Crank, J. 1975. The Mathematics of Diffusion. Oxford University Press, Oxford.
- DiFranco, M., D. Novo, and J. Vergara. 2002. Characterization of the calcium release domains during excitation contraction coupling in skeletal muscle fibres. *Pflugers Arch. Eur. J. Physiol.* 443:508–519.
- DiFranco, M., M. Quinonez, D. A. DiGregorio, A. M. Kim, R. Pacheco, and J. L. Vergara. 1999. Inverted double-gap isolation chamber for high-resolution calcium fluorimetry in skeletal muscle fibers. *Pflugers Arch.* 438:412–418.
- DiGregorio, D. A., A. Peskoff, and J. L. Vergara. 1999. Measurement of action potential-induced presynaptic calcium domains at a cultured neuromuscular junction. *J. Neurosci.* 19:7846–7859.
- Dulhunty, A. F., P. R. Junankar, and C. Stanhope. 1992. Extra-junctional ryanodine receptors in the terminal cisternae of mammalian skeletal muscle fibres. *Proc. Royal Soc. Lond. Ser. B Biol. Sci.* 247:69–75.
- Ebashi, S., and M. Endo. 1968. Calcium ion and muscle contraction. *Prog. Biophys. Mol. Biol.* 18:123–183.
- Eisenberg, B. 1983. Quantitative ultrastructure of mammalian skeletal muscle. In *Handbook of Physiology: Skeletal Muscle*. D. Peachy, R. Adrian, and S. Greiger, editors. American Physiological Society, Bethesda, MD. pp.355–379.
- Endo, M., M. Tanaka, and Y. Ogawa. 1970. Calcium induced release of calcium from the sarcoplasmic reticulum of skinned skeletal muscle fibres. *Nature.* 228:34–36.
- Escobar, A. L., J. R. Monck, J. M. Fernandez, and J. L. Vergara. 1994. Localization of the site of Ca^{2+} release at the level of a single sarcomere in skeletal muscle fibres. *Nature.* 367:739–741.
- Escobar, A. L., P. Velez, A. M. Kim, F. Cifuentes, M. Fill, and J. L. Vergara. 1997. Kinetic properties of calcium indicators: rapid transient responses to flash photolysis of DM-nitrophen. *Pflugers Arch.* 434:615–631.
- Fabiato, A., and F. Fabiato. 1975. Contractions induced by a calcium-triggered release of calcium from the sarcoplasmic reticulum of single skinned cardiac cells. *J. Physiol.* 249:469–495.
- Felder, E., and C. Franzini-Armstrong. 2002. Type 3 ryanodine receptors of skeletal muscle are segregated in a parajunctional position. *Proc. Natl. Acad. Sci. USA.* 99:1695–1700.
- Franzini-Armstrong, C. 1971. Studies of the triad. II. Penetration of tracers into the junctional gap. *J. Cell Biol.* 49:196–203.
- Franzini-Armstrong, C. 1975. Membrane particles and transmission at the triad. *Fed. Proc.* 34:1382–1389.
- Franzini-Armstrong, C., and D. G. Ferguson. 1985. Density and disposition of Ca^{2+} -ATPase in sarcoplasmic reticulum membrane as determined by shadowing techniques. *Biophys. J.* 48:607–615.
- Franzini-Armstrong, C., F. Protasi, and V. Ramesh. 1998. Comparative ultrastructure of Ca^{2+} release units in skeletal and cardiac muscle. *Ann. N. Y. Acad. Sci.* 853:20–30.
- Harkins, A. B., N. Kurebayashi, and S. M. Baylor. 1993. Resting myoplasmic free calcium in frog skeletal muscle fibers estimated with fluo-3. *Biophys. J.* 65:865–881.
- Hobbie, R. K. 1997. Intermediate Physics for Medicine and Biology. AIP Press, New York.
- Hollingworth, S., C. Soeller, S. M. Baylor, and M. B. Cannell. 2000. Sarcomeric Ca^{2+} gradients during activation of frog skeletal muscle fibres imaged with confocal and two-photon microscopy. *J. Physiol.* 526:551–560.
- Huxley, A. F., and R. Niedergerke. 1958. Measurement of the striations of isolated muscle fibres with the interference microscope. *J. Physiol. (Lond.)* 144:403–425.
- Johnson, J. D., Y. Jiang, and J. A. Rall. 1999. Intracellular EDTA mimics parvalbumin in the promotion of skeletal muscle relaxation. *Biophys. J.* 76:1514–1522.
- Johnson, J. D., R. J. Nakkula, C. Vasulka, and L. B. Smillie. 1994. Modulation of Ca^{2+} exchange with the Ca^{2+} -specific regulatory sites of troponin C. *J. Biol. Chem.* 269:8919–8923.
- Kao, H. P., J. R. Abney, and A. S. Verkman. 1993. Determinants of the translational mobility of a small solute in cell cytoplasm. *J. Cell Biol.* 120:175–184.
- Kim, A. M., and J. L. Vergara. 1998. Fast voltage gating of Ca^{2+} release in frog skeletal muscle revealed by supercharging pulses. *J. Physiol.* 511:509–518.
- Klein, M. G., A. Lacampagne, and M. F. Schneider. 1999. A repetitive mode of activation of discrete Ca^{2+} release events (Ca^{2+} sparks) in frog skeletal muscle fibres. *J. Physiol. (Lond.)* 515:391–411.
- Marx, S. O., K. Ondrias, and A. R. Marks. 1998. Coupled gating between individual skeletal muscle Ca^{2+} release channels (ryanodine receptors). *Science.* 281:818–821.
- Maughan, D. W., and R. E. Godt. 1999. Parvalbumin concentration and diffusion coefficient in frog myoplasm. *J. Muscle Res. Cell Motil.* 20: 199–209.

- Mobley, B. A., and B. R. Eisenberg. 1975. Sizes of components in frog skeletal muscle measured by methods of stereology. *J. Gen. Physiol.* 66:31–45.
- Nagerl, U. V., D. Novo, I. Mody, and J. L. Vergara. 2000. Binding kinetics of calbindin-D(28k) determined by flash photolysis of caged Ca^{2+} . *Biophys. J.* 79:3009–3018.
- Naraghi, M., and E. Neher. 1997. Linearized buffered Ca^{2+} diffusion in microdomains and its implications for calculation of $[\text{Ca}^{2+}]$ at the mouth of a calcium channel. *J. Neurosci.* 17:6961–6973.
- Neher, E. 1998. Vesicle pools and Ca^{2+} microdomains: new tools for understanding their roles in neurotransmitter release. *Neuron.* 20:389–399.
- Novo, D., M. DiFranco, and J. L. Vergara. 2001. A 3-D cylindrical diffusion-reaction model of a single myofibril to study localized calcium signaling in skeletal muscle. *Biophys. J.* 80:377A.
- Novo, D., M. G. DiFranco, and J. L. Vergara. 2002. Comparison between model predictions and localized Ca^{2+} transients in amphibian skeletal muscle fibers. *Biophys. J.* 82:641A.
- Pape, P., D. Jong, and W. K. Chandler. 1995. Calcium release and its voltage dependence in frog cut muscle fibers equilibrated with 20 mM EGTA. *J. Gen. Physiol.* 106:259–336.
- Pape, P. C., D. S. Jong, and W. K. Chandler. 1998. Effects of partial sarcoplasmic reticulum calcium depletion on calcium release in frog cut muscle fibers equilibrated with 20 mM EGTA. *J. Gen. Physiol.* 112:263–295.
- Peaceman, D. W., and H. H. Rachford. 1955. The numerical solution of parabolic and elliptic differential equations. *J. Soc. Indust. Appl. Math.* 3:28–41.
- Peachey, L. D. 1965. The sarcoplasmic reticulum and transverse tubules of the frog's sartorius. *J. Cell Biol.* 25:209–231.
- Press, W. H., S. A. Teukolsky, W. T. Vetterling, and B. P. Flannery. 1996. *Numerical Recipes in FORTRAN 77*. Cambridge University Press, Cambridge, UK.
- Rios, E., and G. Pizarro. 1991. Voltage sensor of excitation-contraction coupling in skeletal muscle. *Physiol. Rev.* 71:849–908.
- Rios, E., M. D. Stern, A. Gonzalez, G. Pizarro, and N. Shirokova. 1999. Calcium release flux underlying Ca^{2+} sparks of frog skeletal muscle. *J. Gen. Physiol.* 114:31–48.
- Smith, G. D. 1985. *Numerical Solution of Partial Differential Equations: Finite Difference Methods*. Clarendon Press, New York, NY/Oxford University Press, Oxford, Oxfordshire, UK.
- Sneyd, J., J. Keizer, and M. J. Sanderson. 1995. Mechanisms of calcium oscillations and waves: a quantitative analysis. *FASEB J.* 9:1463–1472.
- Stern, M. D. 1992. Buffering of calcium in the vicinity of a channel pore. *Cell Calcium.* 13:183–192.
- Timmerman, M. P., and C. C. Ashley. 1986. Fura-2 diffusion and its use as an indicator of transient free calcium changes in single striated muscle cells. *FEBS Lett.* 209:1–8.
- Uttenweiler, D., W. G. Kirsch, E. Schulzke, M. Both, and R. H. Fink. 2002. Model-based analysis of elementary Ca^{2+} release events in skinned mammalian skeletal muscle fibres. *Eur. Biophys. J.* 31:331–340.
- Vergara, J., M. DiFranco, D. Compagnon, and B. A. Suarez-Isla. 1991. Imaging of calcium transients in skeletal muscle fibers. *Biophys. J.* 59:12–24.
- Vergara, J. L., M. DiFranco, and D. Novo. 2001. Dimensions of calcium release domains in frog skeletal muscle fibers. *Proc. SPIE.* 4259:133–143.
- Vilsen, B., and J. P. Andersen. 1992. Deduced amino acid sequence and E1–E2 equilibrium of the sarcoplasmic reticulum Ca^{2+} -ATPase of frog skeletal muscle. Comparison with the Ca^{2+} -ATPase of rabbit fast twitch muscle. *FEBS Lett.* 306:213–218.
- Wagner, J., and J. Keizer. 1994. Effects of rapid buffers on Ca^{2+} diffusion and Ca^{2+} oscillations. *Biophys. J.* 67:447–456.
- Wilson, T. 1990. *Confocal Microscopy*. Academic Press, New York.
- Woods, C. E., and J. L. Vergara. 2002. A combined method for confocal detection of Ca^{2+} signals and fluorescence-recovery-after-photobleaching (FRAP). *Biophys. J.* 82:278A.